Review

Inductive Wireless Power Transfer Systems for Low-Voltage and High-Current Electric Mobility Applications: Review and Design Example

Manh Tuan Tran [1,2], **Sarath Thekkan** [1], **Hakan Polat** [1,2], **Dai-Duong Tran** [1,2], **Mohamed El Baghdadi** [1,2] and **Omar Hegazy** [1,2,*]

[1] MOBI-EPOWERS Research Group, ETEC Department, Vrije Universiteit Brussel (VUB), Pleinlaan 2, 1050 Brussels, Belgium
[2] Flanders Make, Gaston Geenslaan 8, 3001 Heverlee, Belgium
* Correspondence: omar.hegazy@vub.be

Abstract: Along with the technology boom regarding electric vehicles such as lithium-ion batteries, electric motors, and plug-in charging systems, inductive power transfer (IPT) systems have gained more attention from academia and industry in recent years. This article presents a review of the state-of-the-art development of IPT systems, with a focus on low-voltage and high-current electric mobility applications. The fundamental theory, compensation topologies, magnetic coupling structures, power electronic architectures, and control methods are discussed and further considered in terms of several aspects, including efficiency, coil misalignments, and output regulation capability. A 3D finite element software (Ansys Maxwell) is used to validate the magnetic coupler performance. In addition, a 2.5 kW 400/48 V IPT system is proposed to address the challenges of low-voltage and high-current wireless charging systems. In this design, an asymmetrical double-sided LCC compensation topology and a passive current balancing method are proposed to provide excellent current sharing capability in the dual-receiver structures under both resonant component mismatch and misalignment conditions. Finally, the performance of the proposed method is verified by MATLAB/PSIM simulation results.

1. Introduction

1.1. Overview

In addition to the rapid development of renewable energy sources, electric vehicle propulsion systems are becoming increasingly popular in recent years as essential solutions to global warming and climate change. Electric vehicles (EVs) are considered highly efficient, have low maintenance costs, and have zero emission compared to internal combustion engine (ICE) vehicle [1]. However, the long battery charging time, the battery life cycle, and the short-range operation are significant obstacles for EVs and mean that they cannot be used as a substitute for all kinds of ICE vehicles [2]. Research institutions and industry have been addressing the bottleneck of battery and charging technologies for decades and have achieved considerable progress.

In the last two decades, the lithium-ion (Li-ion) battery has dominated the modern EV energy storage device market. Recently, solid-state batteries (SSBs) have emerged as a very promising solution due to faster charging times, longer lifecycles, safer operation, and a higher energy density than that of Li-on batteries. Therefore, SSBs are considered the future of battery electric vehicles (BEVs) [3]. Regarding charging technology for electric mobility systems, plug-in conductive charging is a reliable and effective charging method, in which the battery is charged by connecting the cable physically from the AC unity grid to onboard

chargers (OBCs) [4]. However, conductive charging could be extremely dangerous under certain circumstances such as wet weather conditions, or near gas stations due to sparking while plugging and unplugging [5]. Moreover, the autonomous features of EVs are limited due to charging via a wired connection.

Wireless power transfer (WPT) is a promising alternative method for battery charging that does not require a physical cable connection. Hence, the inconvenience and hazards caused by conductive charging are eliminated. Although the original concept of WPT was first introduced by Nicola Tesla in the early 20th century when he conducted the first experiment in which a light bulb was powered wirelessly by high-frequency AC [6], it took a century for WPT technology to become technically mature and applicable in practical scenarios. There are two types of WPT technologies that are widely used in EV systems, namely inductive power transfer (IPT) [5] and capacitive power transfer (CPT) [7,8]. While IPT uses coupled coils to transfer the power by a time-varying magnetic field, CPT transfers power through the electric field generated by coupled capacitors [9]. Among the attractive advantages of IPT is that a single transmitter can feed multiple receivers, despite the system efficiency being subjected to the position of the loads or receivers [10]. Multi-receiver IPT systems have more than one receiving coil and a single transmitter. Such systems are convenient to supply multiple devices simultaneously. In a multi-transmitter system, a single receiver is fed by multiple transmitters. Many studies considered such systems for the dynamic charging of EVs [11,12]. The stationary IPT system is the main subject of this review paper. The IPT system is generally divided into two categories: closely coupled and loosely coupled. In closely or tightly coupled IPT, the coupling coefficient is greater than 0.5 and the magnetizing inductance is higher than the leakage inductance [13]. By contrast, the magnetizing inductance is lower than the leakage inductance in a loosely coupled IPT system, which has a coupling coefficient of less than 0.5. A schematic block diagram of a typical IPT is described in Figure 1, where the transmitter side is supplied by an AC grid and converted to a DC with the help of an active power factor correction (PFC). The transmitter coil is energized, and impedance is matched by a high-frequency inverter (HFI) and a compensation network. On the receiver side, the receiver coil is placed under the vehicle body, the distance between the transmitter and receiver coil is called the airgap or transfer distance. The induced AC voltage on the receiver side is compensated and converted to DC charging voltage/current by a secondary compensation and rectifier stage. In recent decades, IPT systems for high-voltage 420 V battery EVs have been the main design objective and investigated by numerous publications covering various design aspects, including improving efficiency, output regulation capability, coil design compensation networks, and control strategies [14–17].
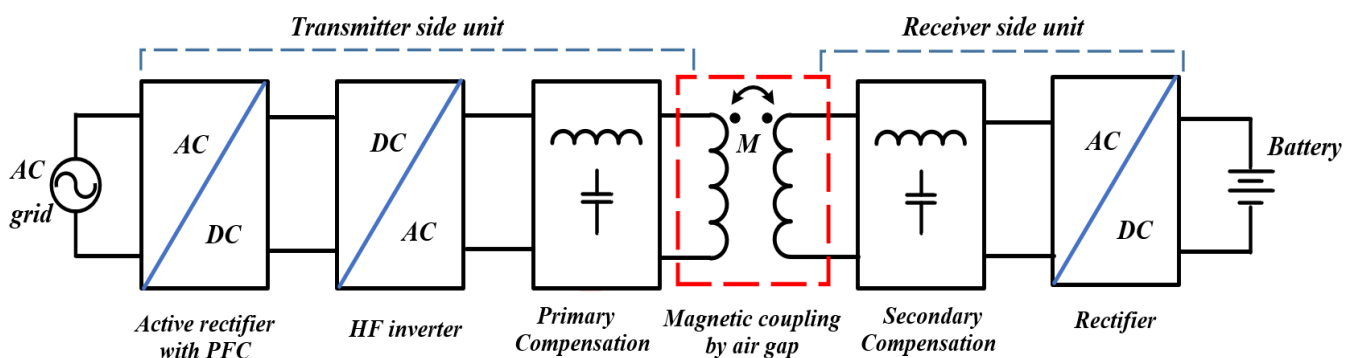
Figure 1. Block diagram of inductive power transfer for electric mobility systems.

1.2. Research Motivation on IPT Systems for Low-Voltage Applications

In urban transportation systems, the transition to low-voltage lithium-ion battery electric vehicle applications such as automated factory logistic vehicles and small-sized urban EVs has accelerated in recent years. As shown in Figure 2, low-voltage IPT systems can be found in a wide range of applications such as light electric vehicles (LEVs), golf

cars, forklifts, electric bikes/motorbikes (E-bikes/motorbikes), Automated Mobile Robots (AMRs), Unmanned Aerial Vehicles (UAVs) and Automated Guided Vehicles (AGVs). According to the market study, micro-EVs have a USD 8.32 billion market share, which is projected to increase to USD 22.11 billion in 2029 as predicted in [18]. Therefore, the micro-EV market is a fast-growing market. Details of a few light-duty EVs working at low-voltage drive trains used for urban mobility off-road applications, and outdoor applications are listed in Table 1. Light electric vehicles (LEVs) are typically equipped with a 48 V battery pack widely employed in urban transportation for last-mile delivery and service applications.
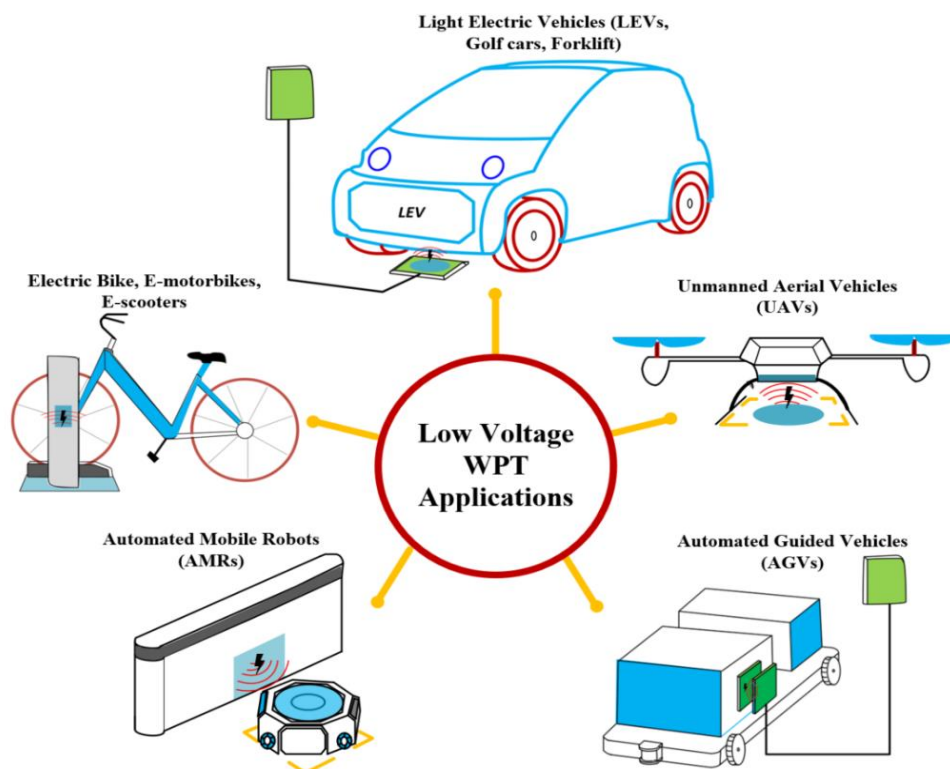

Figure 2. Applications of low-voltage WPT in the mobility sector.

Table 1. Details of different light-duty EVs available in the current markets.

LEVs	Ref.	Motor (kW)	Battery Voltage (V)	Battery Capacity (kWh)	Range (km)	Max Speed (km/h)	Weight (kg)	Use	Country of Origin
Citroen AMI	[19]	6	48	5.5	75	45	485	Urban mobility	France
Renault Twizy	[20]	13	58	6.1	100	80	450	Urban mobility	France
GEM e2	[21]	5	48	8.9	100	40	517	Urban mobility	USA
E-Z-GO Liberty	[22]	8.7	56.7	6.8	NA	31	408	Golf Cart	USA
Italcar-nev C2S.5	[23]	NA	48	NA	120	50	N/A	Urban mobility	Italy
Italcar Attiva fleet.6	[23]	3	48	NA	36	22	N/A	Golf Cart	Italy

Table 1. *Cont.*

LEVs	Ref.	Motor (kW)	Battery Voltage (V)	Battery Capacity (kWh)	Range (km)	Max Speed (km/h)	Weight (kg)	Use	Country of Origin
Polaris Ranger EV	[24]	22	48	14.9	60–70	40	799	Off-road	USA
Club Car Electric	[25]	2.4	48	NA	NA	30	410	Golf Cart	USA
SolidHub GSE2500/5	[26]	11.5	48	34	N/A	15	4000	Forklift	UK
Carver One	[27]	4	48	5,4	100	45.0	330.0	Urban mobility	Netherlands
Microlino	[28]	12.5	N/A	14.0	230	90	530	Urban mobility	Switzerland
Wuling Mini EV	[29]	20.0	90	9.2	120	100	665	Urban mobility	China
Toyota C + Pod	[30]	9.2	177.6	9.1	150	60	680	Urban mobility	Japan
Squad Mobility Solar	[31]	4.0	N/A	6.4	100	45	350	Urban mobility	Netherlands
Tilting Triggo EV	[32]	15	48	14.0	140	90	530	Urban mobility	Poland
Eli Zero	[33]	4.0	72	5.8	80	40	398	Urban mobility	USA

The 48 V electric powertrain system is expected to be a promising urban mobility solution due to its numerous advantages as follows [34,35]:

- From the design perspective, 60 V is considered the upper limit of DC to be safe to touch; and 48 V is safe to touch, hence ground return through the body is possible. Safety and protection requirements are reduced drastically. Further, it is safe to handle the vehicle during any accidents and HV-trained technicians are not needed for maintenance.
- In a 48 V battery, more cells are connected in parallel compared to the high-voltage cells, it is easy to balance the cell voltage and this improves the available energy content.
- Auxiliary components such as turbochargers, intercoolers, HVAC pumps, and EPS motors for 48 V that have already been developed for HEVs can be used.
- No need for additional converters for the auxiliary equipment.
- This voltage level helps to produce better-quality components cost-effectively and reduces overall system costs.

Nevertheless, 48 V drive train systems encounter several difficulties as follows [36–38]:

- It demands a larger amount of current, resulting in higher power losses for the same power level as the high-voltage drive train.
- Cables with a larger diameter are needed, routing of cables inside limited space will be challenging.
- Maximum speed is limited for a 48 V drive train.
- The 48 V system efficiency is low compared to high-voltage systems.

In intralogistics and modern manufacturing processes, Automated Guided Vehicles (AGVs) are the most flexible transport systems due to their ability to move freely through areas and production facilities. Thus, WPT is a necessary technology for AGVs to operate automatically and continuously without human interventions [39,40]. Depending on the applications, AGVs are also equipped with 24 or 48 V batteries [41].

1.3. Paper Contribution and Structure

As mentioned above, a large variety of IPT technical and review articles, mostly focusing on the high-voltage and high-power IPT system for EVs applications have been published over the years [17,42–45]. However, the literature still lacks in-depth reviews, analyses, and updates on compensation topologies, control techniques, and power electronic architectures. Moreover, IPT applications of low voltage and high current have received less attention in the literature. The main contribution of this review paper can be summarized as follows:

(1) This paper intends to provide a review map of compensation selections, control strategies, and power electronic architectures of IPT technology aiming for low-voltage and high-current applications. In which challenges and trends are identified and discussed.

(2) A design concept is proposed as a case study with the verification of Ansys Maxell software and simulation results. In this paper, a high step-down 400 V/48 V IPT system is proposed to address two main issues:

- Firstly, high-current stress on the receiver side and output rectifiers can be reduced due to the proposed asymmetrical compensation structure for the dual-decoupled coils (BP) and LCC-LCC compensation configuration.
- Secondly, the passive current sharing technique is used to significantly improve current balancing between two sets of receiver coils (BP), resonant tanks (LCC-LCC), and output rectifiers under resonant component tolerance and misalignment scenarios. The resonant capacitor and inductor in each receiver are connected in parallel without requiring extra components or control loop design.

As illustrated in Figure 3, this paper is organized as follows: In Section 2, the most popular magnetic coupler structures are briefly outlined and simulated using FEA software. Section 3 delivers a review map including single element, multi-element, and hybrid resonant compensation topologies. Section 4 examines control strategies and power electronic structures to provide an overview of the benefits and drawbacks of each control methodology corresponding to each PE architecture. Section 5 identifies the challenges in designing low-voltage and high-current IPT applications specified for LEVs and AGVs. Afterward, the potential solutions are reviewed and discussed. In Section 6, the design example of a 2.5 kW, 400/48 V IPT system is proposed with the selection of a magnetic coupler structure, design method of compensation network, and PE architecture suitable for LEVs applications. In addition, a passive current balancing technique for a dual decoupled receiver coil system is proposed to address the misalignment tolerance issue. Section 7 is about the further discussion and future works. Lastly, conclusions are presented in Section 8.
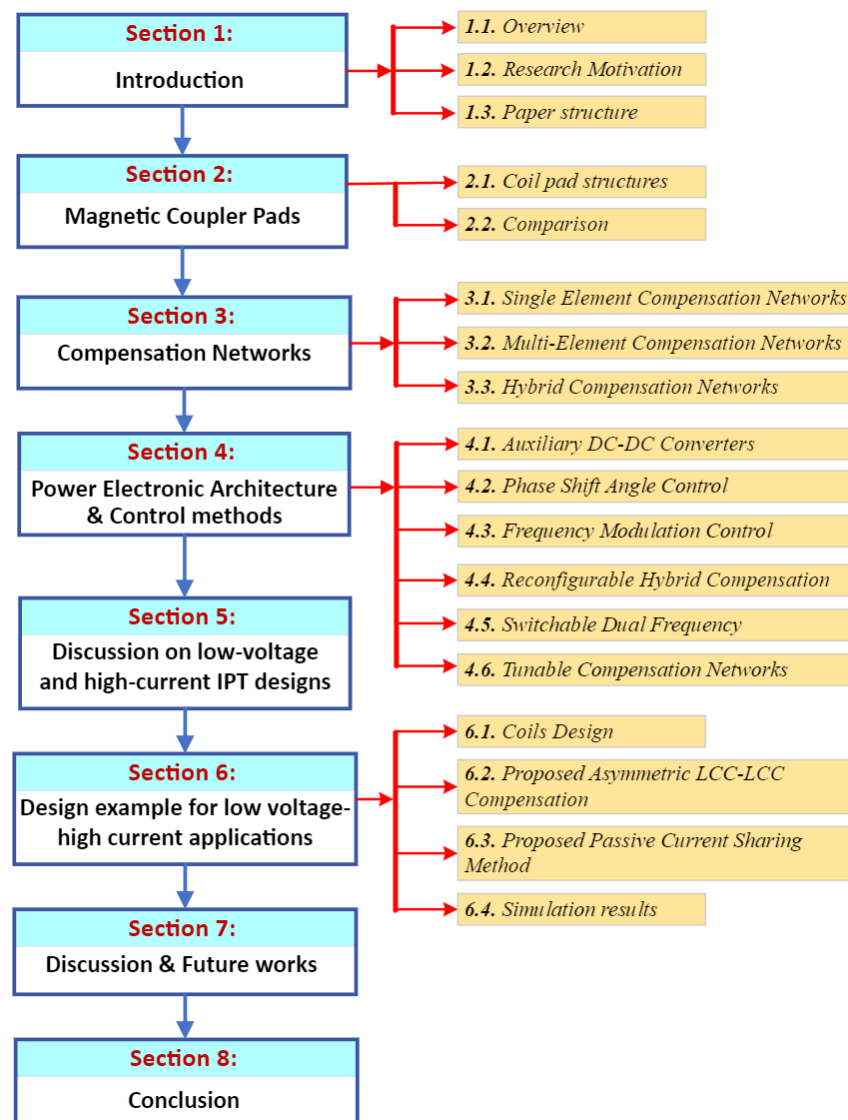
```
┌──────────────────────┐              ┌────────────────────────────────┐
│     Section 1:        │───────────▶ │  1.1. Overview                 │
│     Introduction      │───────────▶ │  1.2. Research Motivation      │
│                       │───────────▶ │  1.3. Paper structure          │
└──────────────────────┘              └────────────────────────────────┘

┌──────────────────────┐              ┌────────────────────────────────┐
│     Section 2:        │───────────▶ │  2.1. Coil pad structures      │
│  Magnetic Coupler Pads│───────────▶ │  2.2. Comparison               │
└──────────────────────┘              └────────────────────────────────┘

┌──────────────────────┐              ┌────────────────────────────────────────┐
│     Section 3:        │───────────▶ │  3.1. Single Element Compensation Networks │
│  Compensation Networks│───────────▶ │  3.2. Multi-Element Compensation Networks  │
│                       │───────────▶ │  3.3. Hybrid Compensation Networks         │
└──────────────────────┘              └────────────────────────────────────────┘

┌──────────────────────┐              ┌────────────────────────────────────────┐
│     Section 4:        │───────────▶ │  4.1. Auxiliary DC-DC Converters           │
│ Power Electronic      │───────────▶ │  4.2. Phase Shift Angle Control            │
│ Architecture &        │───────────▶ │  4.3. Frequency Modulation Control         │
│ Control methods       │───────────▶ │  4.4. Reconfigurable Hybrid Compensation   │
│                       │───────────▶ │  4.5. Switchable Dual Frequency            │
│                       │───────────▶ │  4.6. Tunable Compensation Networks        │
└──────────────────────┘              └────────────────────────────────────────┘

┌──────────────────────┐              ┌────────────────────────────────────────┐
│     Section 5:        │───────────▶ │  6.1. Coils Design                         │
│ Discussion on         │             │  6.2. Proposed Asymmetric LCC-LCC          │
│ low-voltage and       │             │       Compensation                         │
│ high-current IPT      │             │  6.3. Proposed Passive Current Sharing     │
│ designs               │             │       Method                               │
└──────────────────────┘             │  6.4. Simulation results                   │
                                      └────────────────────────────────────────┘
┌──────────────────────┐
│     Section 6:        │
│ Design example for    │
│ low voltage-high      │
│ current applications  │
└──────────────────────┘

┌──────────────────────┐
│     Section 7:        │
│ Discussion & Future   │
│ works                 │
└──────────────────────┘

┌──────────────────────┐
│     Section 8:        │
│     Conclusion        │
└──────────────────────┘
```

Figure 3. The organizational structure of this paper.

2. Magnetic Coupler Pads

As transformers in power converters, the magnetic coupler pad plays a critical role in wireless power transmission systems. It consists of two coils, namely the transmitter, and receiver, separated by an air gap. The key performance parameters of the magnetic structure are self-inductance, mutual inductance or coupling coefficient, and quality factor. A compact and lightweight coil with high efficiency, a large air gap, and good misalignment tolerance in the lateral direction are the required features of the IPT coils for EVs [14]. For a simple coil geometry with air core coils, the self and mutual inductance of the coupler pad can be derived by analytical expressions. However, deriving analytical equations of complex geometry coil structures with magnetic shielding is impractical. Hence, the finite element analysis (FEA) tool becomes a feasible solution to acquire coils parameters and validated coils performance. Furthermore, the electromagnetic flux distribution surrounding the coil can be visualized to aid in the verification of the coil design. According to [46], the power output can be defined in terms of the open-circuit voltage V_{oc}, short circuit current I_{sc}, and the receiver-side quality factor Q as in Equation (1).

$$P_{out} = P_{su}Q = V_{oc}I_{sc}Q = \omega M I_1 \frac{M I_1}{L_2} Q = \omega I_1{}^2 \frac{M^2}{L_2} Q \qquad (1)$$

where M is the mutual inductance between the coils, I_1 is the primary side current and L_2 is the self-inductance of the receiver coil. Power output can be increased by primary current, frequency, quality factor Q, or by optimizing magnetic design. Input current and frequency are limited by the power electronics components and the Litz wire [47]. Hence, an improved magnetic design is an effective method to improve the power output. The magnetic design parameters, mutual inductance M are determined by the distance between the coils and the alignment of the coils while L_2 purely depends on the geometry of the respective coil [14]. Therefore, designing IPT coils is a crucial step, which includes the airgap distance, coil shape, material selection, and conductor selection.

In these mutually coupled coils, a higher coupling coefficient results in higher efficiency. The coupling coefficient k, represented as $k = M/\sqrt{L_1 L_2}$, demonstrates the magnetic coupling strength between self-inductance of transmitter L_1 and receiver L_2. Ferrites bars or ferrite plates are used to improve the coupling coefficient by modifying the flux path. As a result, both self-inductance and mutual inductance can be increased. Another feature of inserting the ferrite bar into the magnetic coupler is that it limits magnetic radiation and EMI disturbance. MnZn and NiZn are two common ferrite materials used for manufacturing ferrite [48]. During operation, the saturation of the ferrite should be avoided, which means it should operate in the linear region. Saturation reduces permeability and decreases coil inductance, which detunes the compensation circuits. Ferrite core can almost double the self-inductance of the coils and increase the coupling coefficient by 30–50%, considering the same transfer distance [49].

The quality factor, $Q = \omega L/R$ describes the resonance behavior of an under-damped harmonic oscillator [50]. It shows the pure inductiveness of the coil and signifies the ability to produce a large magnetic field [51].

Since the leakage magnetic field creates an adverse effect on humans and surrounding metallic objects, safety criteria need to be considered. Therefore, designing coil pad need to meet electromagnetic interference (EMI) and EMC standard [52]. An aluminum shield is attached to the backside of the ferrite bars and coil as shown in Figure 4. This shielding technique is to absorb the leakage magnetic field. However, the power losses of the IPT system are increased due to eddy currents induced in the shielding sheets [53].
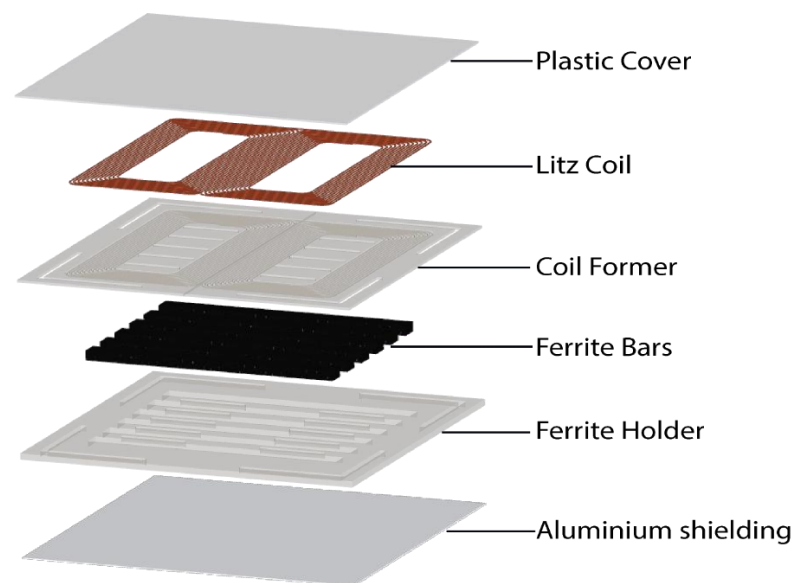
Figure 4. Exploded view of DD coil pad with accessories.

2.1. Coil Pad Structures

In this review, the magnetic coupler structures for stationary IPT systems are considered. High-current stress and compactness are the major difficulties in designing coil

pads for LEVs and AGV applications. As depicted in Figure 5, several coil structures are reviewed to find suitable solutions for low-voltage and high-current IPT applications.

- A circular pad generates a single-sided, unipolar magnetic field, which is preferred in IPT for EV applications [14]. It is the most common coil structure due to its features such as symmetry, simplicity to manufacture, and analyses [50,54].
- A planar spiral coil with a square or rectangular shape is called a square/rectangular coil and is considered a closed variant of CP [50]. Therefore, it is also a suitable coil structure for EV chargers due to the convenience of installation. This coil structure is also simple to manufacture and shows symmetric characteristics. Better lateral misalignment tolerance compared to the circular coil. Lateral tolerance is higher along the longer side than the shorter side [55].
- In circular, rectangular, square, and helical coil structures, only a pair of coils is used for coupling. Budhia et al. [16,56] proposed a double D (DD) coil system as shown in Figure 5c. The flux generated by this structure is bipolar and single sided in nature, this coil configuration shows better performance than unipolar pads such as circular and rectangular [47]. In addition, the fundamental height of the flux path is proportional to half the length of the pad resulting in a higher coupling coefficient called intra-pad coupling [16]. These coils are magnetically in parallel and electrically in series. Thus, the unwanted leakage flux path at the rear side of the coil pairs is reduced. DD pad is commonly used as a transmitter and has interoperable with different receiver topologies. However, the conductor length and ohmic loss are higher, so it is not suitable to be applied on the receiver side of low-voltage and high-current IPT systems. The self-inductance of the DD coil is almost 1.7 times the self-inductance of the rectangular coil with the same dimension.
- DD coil only couples the horizontal component of the flux. Misalignment tolerance can be improved further by placing a third coil in the DD coil's center. This third coil is aligned in special quadrature to the DD coils, and it helps to capture perpendicular flux [56]. This three-coil structure is a modified version of the DD structure called DDQ as shown in Figure 5d. In a perfectly designed DDQ coil, the series connected DD coil and the Q coils are mutually decoupled so these can be tuned and controlled separately [48]. It is demonstrated that the charging zone of the DDQ system is five times larger than that of a circular pad of comparable size [16]. However, DDQ requires more copper wire compared to others and complex design process.
- A bipolar (BP) coil is a multi-coil configuration with a bipolar flux path. There are two identical, partially overlapped coils in a BP pad. The top view and simulation model of the BDD coil are shown in Figure 5e. It is commonly adopted on the secondary side. Overlapping of two similar coils helps to cancel out the flux, this concept is used to achieve the decoupling [57]. The superior characteristics BP coil are the remarkable increase in the charging zone and the lateral misalignment tolerance. The benefit of such decoupled coils is that they can be tuned and regulated separately.

2.2. Comparison

In this study, circular, rectangular, DD, and BP coils with ferrite bars are designed with the same outer dimension of 400 × 400 mm, 100 mm air gap, and simulated by Ansys Maxwell. The lateral misalignment tolerance of circular, rectangular, DD, and BP are investigated in this section. All models are simulated under different lateral misalignments varying from 5% to 30%, corresponding to a misalignment range of 120 mm. From Figure 6, it can be observed that the BP coil structure has the strongest coupling coefficient and best misalignment tolerance, followed by the DD, rectangular, and circular pads. The lateral misalignment tolerance of rectangular and circular are nearly similar. BP achieves similar lateral misalignment tolerance to DDQ by overlapping instead of using an extra coil, requiring fewer copper coils.
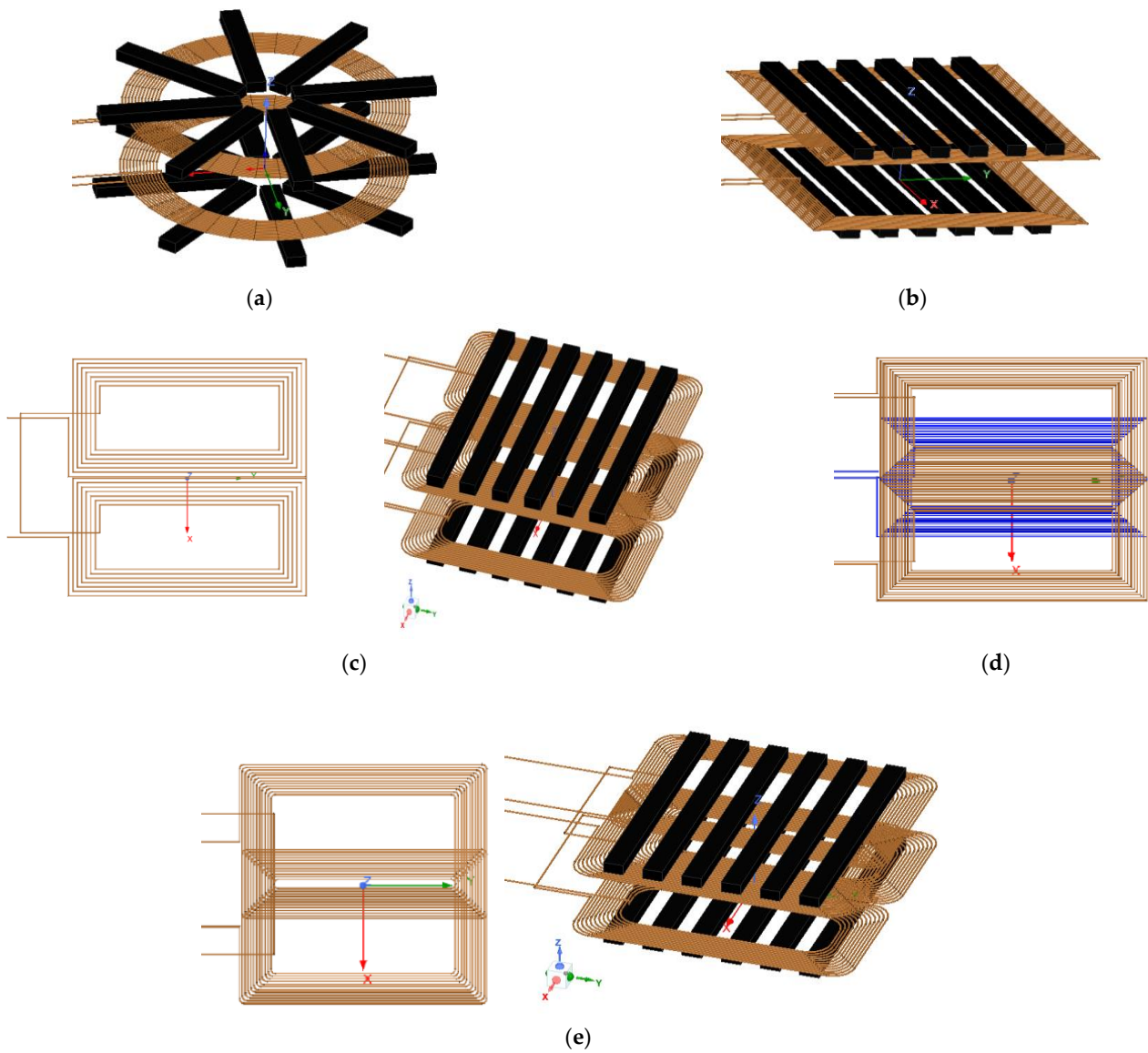
Figure 5. Different pads structures for static IPT systems. (**a**) Circular pad. (**b**) Rectangular pad. (**c**) DD pad. (**d**) DDQ pad. (**e**) BP pad.
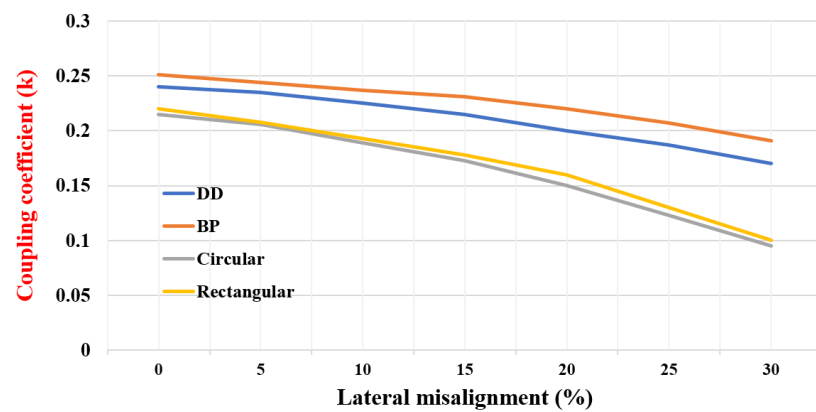

Figure 6. Comparison performance of different coils under various lateral misalignment conditions.

As presented in [47], the BP coil used 25.17% less copper than the DDQ design with the same dimension. In this simulation setup, the circular requires the shortest conductor length of 14 m and DDQ needs the longest conductor length of 27 m. According to a variety of previous works, the performance comparison among four coil structures is summarized and tabulated in Table 2.

Table 2. Comparison of different types of coils [5,14,16,54–58].

	Circular	Rectangular/Square	DD	DDQ	BP
Number of coils	1	1	1	2	2
Flux type	Single sided and unipolar	Single sided and unipolar	Single sided and bipolar	Double sided and bipolar	Double sided and bipolar
Flux leakage	High	Moderate	Very low	Very low	Very low
Transfer distance	Low	Low	Moderate	Large	Large
Misalignment tolerance	Very poor	Poor	Good	Better	Better
Interoperability	Poor	Poor	Good	Best	Best
Charging area	Small	Small	Moderate	Large	Large
Commonly used as	Tx/Rx	Tx/Rx	Tx	Rx	Rx
ESR Losses	Small	Small	Medium	Large	Large
Complexity	Very simple	Very simple	Simple	Complex	Moderate

3. Compensation Networks

To clarify the role of the compensator in the IPT systems, it is necessary to first understand the system without compensation. A loosely coupled transformer model with large leakage inductance and low mutual inductance is utilized for modeling primary and secondary coils placed at a relatively large distance. Figure 7a is the representation of the IPT system, and the mutual inductance model is depicted in Figure 7b, where L_P, L_S, and M are the self-inductances of primary and secondary coils and the mutual inductance between the coils respectively. Primary and secondary coil resistances are represented by R_P and R_s respectively. V_{in} is the supply voltage with a frequency ω, much smaller than the self-resonating frequency. Hence, the stray capacitance can be neglected. In Figure 7c, the input impedance Z_{in} is calculated by reflecting the equivalent impedance from the secondary side into the primary side by Equation (2) and the efficiency is the ratio of the power available at the load to the power supplied by the source, which are expressed by Equation (3) [59].

$$Z_{in} = \frac{\omega^2 M^2 + (R_P + j\omega L_P)(R_L + R_S + j\omega L_S)}{R_S + j\omega L_S + R_L} \tag{2}$$

$$\begin{cases} \eta_{link} = \frac{R_L}{(R_L+R_S)(1+R_P\frac{R_L+R_S}{\omega^2 M^2})+R_P(\frac{L_P}{M})^2} \\ \eta_{link,max} = \frac{R_L}{(R_L+R_S)+R_P(\frac{L_P}{M})^2} \\ when \; \omega \gg \frac{\sqrt{R_P(R_L+R_S)}}{M} \end{cases} \tag{3}$$
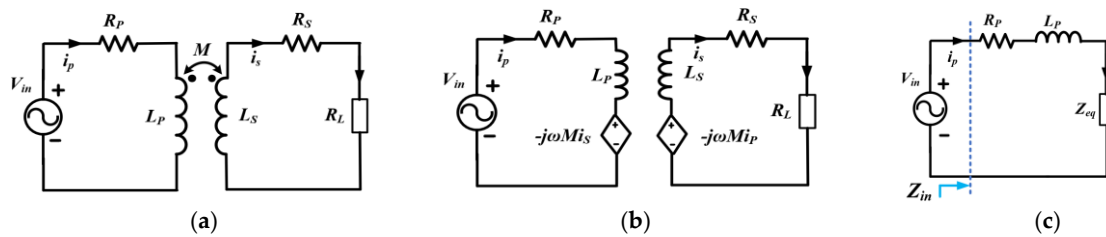
Figure 7. General IPT system without compensators, (**a**,**b**) circuit diagram of mutual inductance model, and (**c**) equivalent circuit reflected in the primary side.

It can be noticed from Equation (3) that maximum efficiency can be achieved by increasing operating frequency. However, the input impedance Z_{in} becomes very high and more inductive. This results in a low power factor. It means that the high-frequency inverter (HFI) and the rectifier should have a high VA rating and significant power losses [59]. This bottleneck of IPT in the absence of compensations can be overcome by integrating compensator networks to minimize the circulation of high reactive current [60].

Typically, compensator networks are the combinations of capacitors and inductors connected to form different resonant topologies [44,61,62]. Compensation plays crucial roles in the IPT systems in several aspects such as:

- Minimized reactive circulating current by canceling leakage inductance in the primary HFI and secondary rectifier. As a result, maximum power transfer and system efficiency are achieved.
- Allow high switching operation due to soft-switching characteristics such as zero voltage switching (ZVS) and zero current switching (ZCS) in power devices.
- Avoid bifurcation and increase the tolerance of the system for misalignment [60].
- Implement constant current (CC) or constant voltage (CV), which is suitable for battery charging of EV applications [42].
- Improving the misalignment tolerance [63].

Compensation topologies have been extensively studied in terms of the aforementioned features since they are a critical part with a significant impact on system stability and efficiency. Compensation topologies can be classified into single-element-resonant, multi-element resonant compensation networks, and hybrid reconfigurable compensators. This review paper also investigates in more detail the principles of achieving constant-current (CC) or constant-voltage (CV) output based on the load-independent characteristic of different resonant networks [42]. A suitable compensation is required to maintain a stable output regardless of load conditions. In addition load-independent features, zero phase angle (ZPA) is also a critical criterion affecting the efficiency of whole IPT systems.

ZPA can be achieved as there is no imagine part in the primary-reflected impedance Z_{in}. The phase angle between the input voltage and current is expressed in Equation (4).

$$\theta_{in} = \frac{180}{\pi} tan^{-1} \frac{Im(Z_{in})}{Re(Z_{in})} \tag{4}$$

ZPA can be obtained $\theta_{in} = 0$ when $Im(Z_{in}) = 0$. Each topology has advantages and disadvantages in terms of simplicity, efficiency, and misalignment tolerance. Therefore, suitable resonant topologies are selected to satisfy the requirements of different IPT applications. It is preferable to design θ_{in} slightly greater than zero to ensure the soft-switching operation of the primary switches.

3.1. Single Element Compensation Networks

The four basic and simple combinations are series–series (SS), series–parallel (SP), parallel–series (PS), and parallel-parallel (PP). The naming is such that the first part represents the way the compensation capacitor is connected to the primary side coil and the second one on the secondary side. The circuit diagrams of basic topologies are shown in

Figure 8, where C_1 and C_2 are primary compensation capacitance, and secondary compensation capacitance, respectively. Figure 8a shows the circuit configuration of the S-S topology. It is superior among these four topologies since its resonance frequency and the coupling coefficient are not dependent on load conditions. Additionally, it can provide constant current CC under ZPA conditions with minimum component count [64–67].
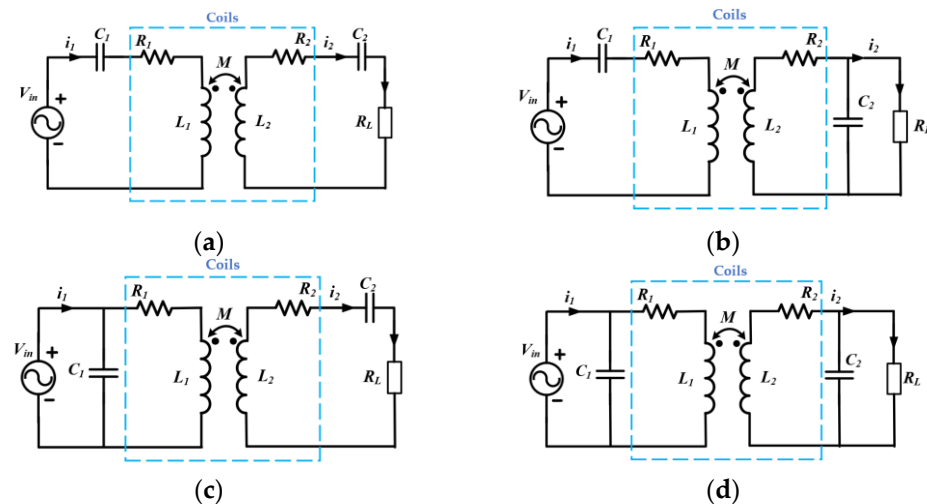

Figure 8. Single-element resonant compensations. (**a**) Series–series. (**b**) Series–parallel. (**c**) Parallel–series. (**d**) Parallel-parallel.

However, the coupling coefficient has a strong influence on the output current, resulting in a highly sensitive system. Since the input impedance is inversely proportional to the mutual inductance value. The input current becomes extremely large when the receiver is absent. Primary series and secondary parallel (SP) compensation are designed to provide a constant-voltage output under ZPA condition as shown in Figure 8b. As the same disadvantage as the SS compensator, SP topology impedance reaches zero at resonant frequency when the receiver is not presented. Thus, the input current protection method needs to apply for preventing short circuit [64,68,69].

As shown in Figure 8c,d, the transmitter side capacitors C_1 are connected in parallel with transmitter coil L_1. Therefore, this circuit configuration is normally driven by a current source. Presently, the mainstream of IPT systems is widely adopted by a primary voltage source, which makes PP and PS become unpopular and less attractive compensation networks [44]. It can be observed that single-element compensations have the simplest circuit structure. Therefore, they are preferred for high-current secondary side applications. The major disadvantages of low-order resonant networks are lacking the degree of freedom (DOF) and output fluctuation due to misalignment conditions.

3.2. Multi-Element Compensation Networks

In order to extend the operating condition and improve the performance of single-element topologies, multi-element resonant networks consisting of multiple energy store elements are extensively investigated in previous works. To overcome the problem of the voltage source in PS, PS topologies, Qu et al. [65] proposed a solution, in which an additional inductor L_x is connected between the voltage source and primary parallel capacitor to create three-element compensators called PP, PS with L_x as shown in Figure 9a,b. Meanwhile, PS with L_x can obtain CV and ZPA, PP with L_x can deliver CC under ZPA condition. Nevertheless, DOF of those topologies still is restricted by self-inductance and mutual inductance value as presented in Table 3. To improve the fluctuation output of single-element topologies due to the variation of parameters, the series/series-parallel (S/SP) has been introduced as shown in Figure 9c [70–74]. The CV and ZPA features are maintained with small deviations under misalignment conditions. Due to lacking DOF, S/SP is suitable for the voltage gain of unity with symmetrical coils [74]. Therefore, it

brings more difficulties in designing high step-down IPT systems such as LEVs and AGV applications. To further extend the DOF of IPT systems, more resonant components are added to form high-order resonant topologies. Figure 9d–h show topologies of LC-LC, S-LCC, LCC-S, LCC-P, and LCC-LCC. Which are commonly used in numerous research works. Double-side LC-LC, also called LCL-LCL compensation, shown in Figure 9d, where four external resonant components form a symmetrical structure, LC-LC owns the characteristic of CC and ZPA at resonant frequency [75]. The drawback of LC-LC is still constrained by coil parameters [76]. Asymmetrical four-element topologies of S-LCC and LCC-S can provide CV output at ZPA resonant frequency as depicted in Figure 9e,f.
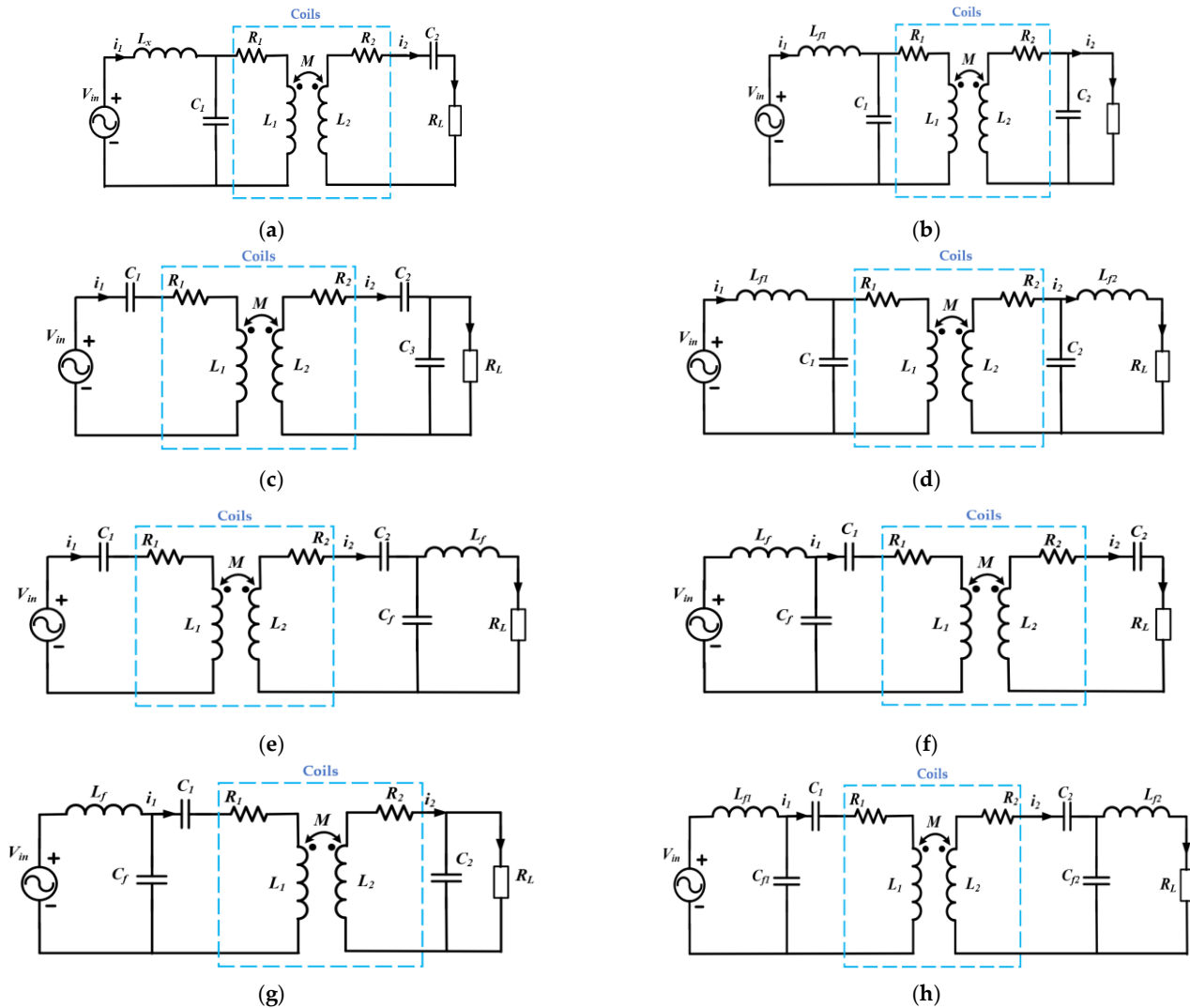
Figure 9. Multi-element resonant compensations. (**a**) PS with L_x. (**b**) PP with L_x. (**c**) Series/series–parallel (S/SP). (**d**) LC-LC (LCL-LCL). (**e**) S-LCC. (**f**) LCC-S. (**g**) LCC-P. (**h**) LCC-LCC.

In contrast to S/SP, in which the CV value is heavily influenced by the turn ratio of the transmitter and receiver coils, the voltages of S-LCC and LCC-S can be defined independently by selecting the external value L_f. The load-independent voltage of S-LCC is proportional to the coupling coefficient [77–79]. Meanwhile, the constant voltage value is inversely proportional to the coupling coefficient in the LCC-S topology [80,81].

Table 3. Load-independent characteristics of different compensation networks.

Compensation Topologies	Operating Resonant Frequency	Output Characteristics	Load Output	ZPA
SS [64–67]	$f_o = \frac{1}{2\pi\sqrt{L_1 C_1}} = \frac{1}{2\pi\sqrt{L_2 C_2}}$	CC	$i_O = \frac{V_{in}}{\omega_o M}$	Yes
SP [68]	$f_o = \frac{1}{2\pi\sqrt{(L_1 - \frac{M^2}{L_2})C_1}} = \frac{1}{2\pi\sqrt{L_2 C_2}}$ Resonant frequency-coupling dependent	CV	$V_O = \frac{V_{in} L_2}{M}$	Yes
PS with L_x [65]	$f_o = \frac{1}{2\pi\sqrt{L_1 C_1}} = \frac{1}{2\pi\sqrt{L_2 C_2}}$ And $L_1 = L_x$	CV	$V_O = \frac{V_{in} M}{L_2}$	Yes
PP with L_x [65]	$f_o = \frac{1}{2\pi\sqrt{(L_1 - \frac{M^2}{L_2})C_1}} = \frac{1}{2\pi\sqrt{L_2 C_2}}$ And $L_x = L_1 - \frac{M^2}{L_2}$ Resonant frequency-coupling dependent	CC	$i_O = \frac{M V_{in}}{\omega_o(L_1 - \frac{M^2}{L_2})L_2}$	Yes
S/SP [70–74]	$f_o = \frac{1}{2\pi\sqrt{L_1 C_1}} = \frac{1}{2\pi\sqrt{L_2 C_2}} = \frac{1}{2\pi\sqrt{L_M C_3}}$ Resonant frequency-coupling dependent	CV	$V_O = V_{in}$	Yes
LC-LC [75,76]	$f_o = \frac{1}{2\pi\sqrt{L_1 C_1}} = \frac{1}{2\pi\sqrt{L_2 C_2}}$ And $L_1 = L_{f1}, L_2 = L_{f2}$	CC	$i_O = \frac{M V_{in}}{\omega_o L_{f1} L_{f2}}$	Yes
S-LCC [77–79]	$f_o = \frac{1}{2\pi\sqrt{L_1 C_1}} = \frac{1}{2\pi\sqrt{L_f C_f}} = \frac{1}{2\pi\sqrt{(L_2 - L_f)C_2}}$	CV	$V_O = \frac{V_{in} L_f}{M}$	Yes
LCC-S [80,81]	$f_o = \frac{1}{2\pi\sqrt{L_2 C_2}} = \frac{1}{2\pi\sqrt{L_f C_f}} = \frac{1}{2\pi\sqrt{(L_1 - L_f)C_1}}$	CV	$V_O = \frac{V_{in} M}{L_f}$	Yes
LCC-P [82–85]	$f_o = \frac{1}{2\pi\sqrt{L_f C_f}} = \frac{1}{2\pi\sqrt{L_2 C_2}} = \frac{1}{2\pi\sqrt{(L_1 - L_f - \frac{M^2}{L_2})C_1}}$ Resonant frequency-coupling dependent	CC	$i_O = \frac{M V_{in}}{\omega_o L_f L_2}$	Yes
LCC-LCC [86–90]	$f_o = \frac{1}{2\pi\sqrt{L_{f1} C_{f1}}} = \frac{1}{2\pi\sqrt{L_{f2} C_{f2}}} = \frac{1}{2\pi\sqrt{(L_1 - L_{f1})C_1}} = \frac{1}{2\pi\sqrt{(L_2 - L_{f2})C_2}}$	CC	$i_O = \frac{M V_{in}}{\omega_o L_{f1} L_{f2}}$	Yes

The LCC-P compensation can provide constant current CC output [82–85]. Kavimandan et al. [84] conducted a sensitive analysis of LCC-S and LCC-P and concluded that the voltage stress across C_{f1} and C_2 of LCC-P is lower than that of LCC-S while voltage stress across C_1 is higher for LCC-P. Additionally, input current is reduced in LCC-S and increased in LCC-P when the receiver coil shifts away from transmitter. Thus, LCC-S is more suitable than LCC-P in static and dynamic IPT system under high misalignment conditions. LCC-LCC compensation is the most popular high-order topology investigated in several works [86–90]. As shown in Figure 9h, two LCC circuit configurations are inserted on both sides of the coil structure. Since the number of storage components increases, the circuits have multiple resonating frequencies as shown in Figure 10, depicting the frequency response of LCC-LCC compensation. Compared to other topologies, double-side LCC has outstanding performances in several aspects such as small output variation, high misalignment tolerances, safety operation under zero coupling and null-load conditions, good efficiency, and bi-directional operation. Moreover, LCC-LCC topology can offer both CC and CV at two different ZPA frequencies, making it more attractive to be applied in battery EV charging applications [89,90]. Nevertheless, this resonant topology uses large

numbers of passive components, it is not the best candidate for a high demand on power density. To improve the power density, the external inductors are integrated with the magnetic coupling structure as proposed in [88,91]. However, integrated magnetic coupling demands a complex design process to the minimum coupling between the main coils and resonant inductors. Table 3 summarizes the load-independent characteristics of the most studied topologies, including single-element and multi-element resonant compensations.
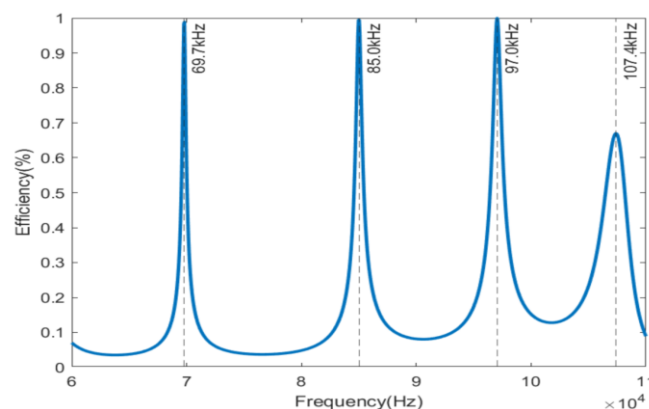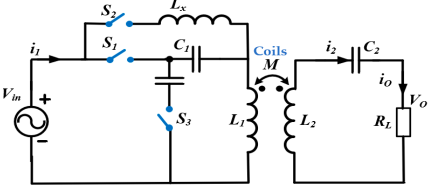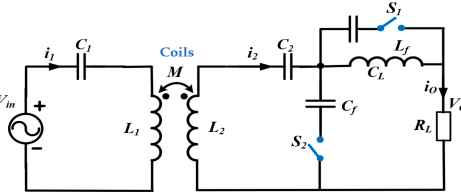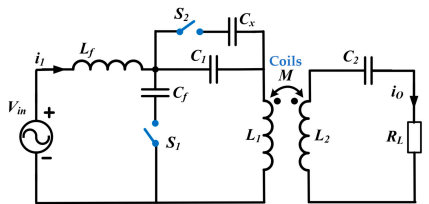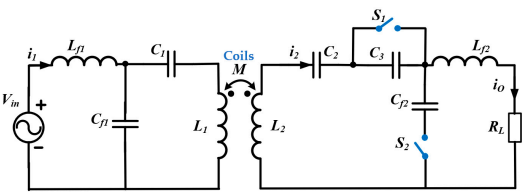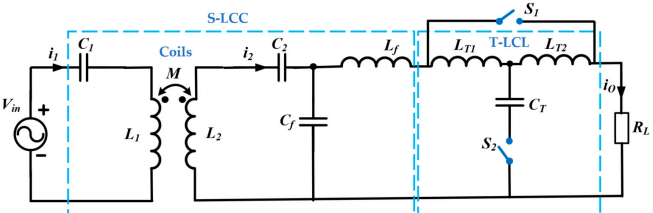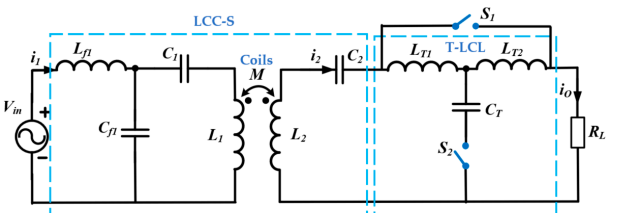
Figure 10. Frequency response of LCC-LCC topology.

3.3. Hybrid Compensation Networks

The charge process for lithium batteries normally includes constant current (CC) charge and constant voltage (CV) charge to fully charge the batteries. Initially, the battery is charged with a constant current and the battery voltage increases gradually during this mode. When the battery voltage reaches the maximum charge voltage, the battery is charged by the CV mode.

Several topologies are inherent characteristics of ZPA input and load-independent CC or CV output as reported in Sections 3.1 and 3.2. To exploit the natural CC/CV operation of compensations for IPT battery charging, the hybrid reconfigurable resonant networks approach is widely used for IPT battery charging applications due to load-independent and ZPA characteristics. The idea behind this approach is the combination of two load-independent CC and CV topologies operating at the same resonant frequency under ZPA conditions. By switching between two circuit configurations, CC/CV is automatically implemented with low reactive power in the entire range of load conditions [65,79,92–96]. Depending on the required design parameters, low-order or high-order resonant networks can be selected as depicted in Table 4. In [65,68], the CC/CV charging profile can be simply implemented by switching between two low-order topologies such as SS and SP. However, there is a limitation in degrees of freedom to satisfy all IPT applications since output parameters heavily depend on mutual inductance M. To overcome the design constraint of low-order compensations, the high-order hybrid topologies are constructed by employing LCC-S and S-LCC for CV mode, while still lacking design freedom in CC mode [92]. Hence, LCC-LCC can be adopted for performing CC charging by selecting two independent variables L_1 and L_2 [94]. On the other hand, it is also well known that a T-type LCL network is able to convert a constant voltage source into a constant current source and vice versa. Therefore, it is cascaded after LCC-S or S-LCC topology to realize CC operation [79,95]. The additional resonant components and ACSs are preferred to locate on receiver side to avoid using wireless communication link between two sides. However, this circuit configuration induces larger losses for low-voltage and high-current IPT systems. Moreover, receiver pads are equipped in vehicles. Hence, fewer passive components on the receiver side are highly recommended.

Table 4. Reconfigurable hybrid topologies with constant current and constant voltage configurations.

Reconfigurable Hybrid Topologies	Mode Selections	
	CC Mode	**CV Mode**
[65]	S1: ON and S2, S3: OFF SS $i_O = \frac{V_{in}}{\omega_o M}$ ZPA: Yes	S1: OFF and S2, S3: OFF PS with L_x $V_O = \frac{V_{in} M}{L_2}$ $(L_1 = L_x)$ ZPA: Yes
[92]	S1: ON, S2: OFF SS $i_O = \frac{V_{in}}{\omega_o M}$ ZPA: Yes	S1: OFF, S2: ON S-LCC $V_O = \frac{V_{in} L_f}{M}$ ZPA: Yes
[93]	S1: OFF, S2: ON SS $i_O = \frac{V_{in}}{\omega_o M}$ ZPA: Yes	S1: ON, S2: OFF LCC-S $V_O = \frac{V_{in} M}{L_f}$ ZPA: Yes
[94]	S1: OFF, S2: ON LCC-LCC $i_O = \frac{M V_{in}}{\omega_o L_{f1} L_{f2}}$ ZPA: Yes	S1: ON, S2: OFF LCC-S $V_O = \frac{V_{in} M}{L_{f1}}$ ZPA: Yes
[79]	S1: OFF, S2: ON S-LCC+LCL $I_O = \frac{V_{in} L_f}{M \omega_o L_T}$ $(L_{T1} = L_{T2} = L_T)$ ZPA: Yes	S1: ON, S2: OFF S-LCC $V_O = \frac{V_{in} L_f}{M}$ ZPA: Yes
[95]	S1: OFF, S2: ON LCC-S+LCL $I_O = \frac{M V_{in}}{\omega_o L_f L_T}$ $(L_{T1} = L_{T2} = L_T)$ ZPA: Yes	S1: ON, S2: OFF LCC-S $V_O = \frac{V_{in} M}{L_f}$ ZPA: Yes

4. Power Electronic Architectures and Control Methods

In this section, an overview of power electronic architectures and control methodologies for static IPT systems are presented to identify the current trends published in massive works. In a typical IPT system, maximum efficiency tracking (MET) and output regulation capacities including CC/CV implementation are the most dominant control objectives in various charging applications. For an IPT system, the most effective and safe charging procedure for Li-on battery packs is CC/CV charging profile, which maintains constant current (CC) and constant voltage (CV) modes. In addition, the equivalent battery resistance varies during the charging time. Hence, the maximum efficiency tracking technique based on the principle of matching source and load impedance is needed to maximize the IPT system's efficiency.

Thus, a variety of control strategies are proposed to deal with these matters, corresponding to a diversity of power electronic structures. As briefly depicted in Figure 1, the transmitter side power electronics basically consists of a front-end PFC, a high-frequency inverter, and a compensation network. While the receiver side consists of a compensation network and a rectifier to convert high-frequency ac voltage into dc voltage. However, these typical PE structures are greatly modified for different control strategies to fulfill the output requirements of output regulation and efficiency maximization as classified in Figure 11 and summarized in Table 5. Generally, these control strategies can be classified into several types: adding an auxiliary dc-dc converter, variable frequency, variable phase shift, switchable frequency, reconfigurable resonant compensations, and tunable resonant networks.
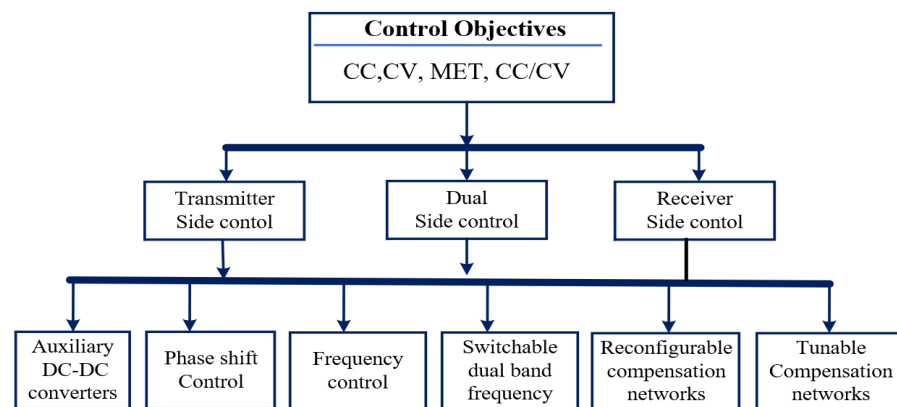
Figure 11. Category of control strategies in the IPT systems.

Table 5. Summary of control methodologies for IPT systems.

Control Methodologies	Primary Side (HB, FB)	Secondary Side (AR, Semi-R, PR)	Dual Side
Frequency tuning	CP [97] MET [98] CC/CV [99]	N/A	N/A
Phase shift control	CC/CV [100]	CC/CV [101,102]	CC/CV [103] CC/CV + MET [104]
Auxiliary DC-DC converter (Buck, Boost, Boost-Buck)	CC/CV [105]	MET [106–108]	MET + CV [109–111]
Switchable dual-band frequency	CC/CV [89,90,112]	N/A	N/A
Reconfigurable compensation networks	CC/CV [65,93]	CC/CV [79,87,92,94,95]	
Tunable compensation networks (Tunable equivalent capacitances or inductances)	MET [113,114] CC/CV [115,116]	CC/CV [117]	CC [118] CP [119]

CP: constant power, MET: maximum efficiency tracking.

4.1. Auxiliary DC-DC Converters

For IPT systems, auxiliary dc-dc converters are widely used to achieve output regulation and impedance-matching capabilities. Figure 12 shows the circuit diagrams, in which dc-dc converter can be adopted on the receiver side, transmitter side, or both sides.
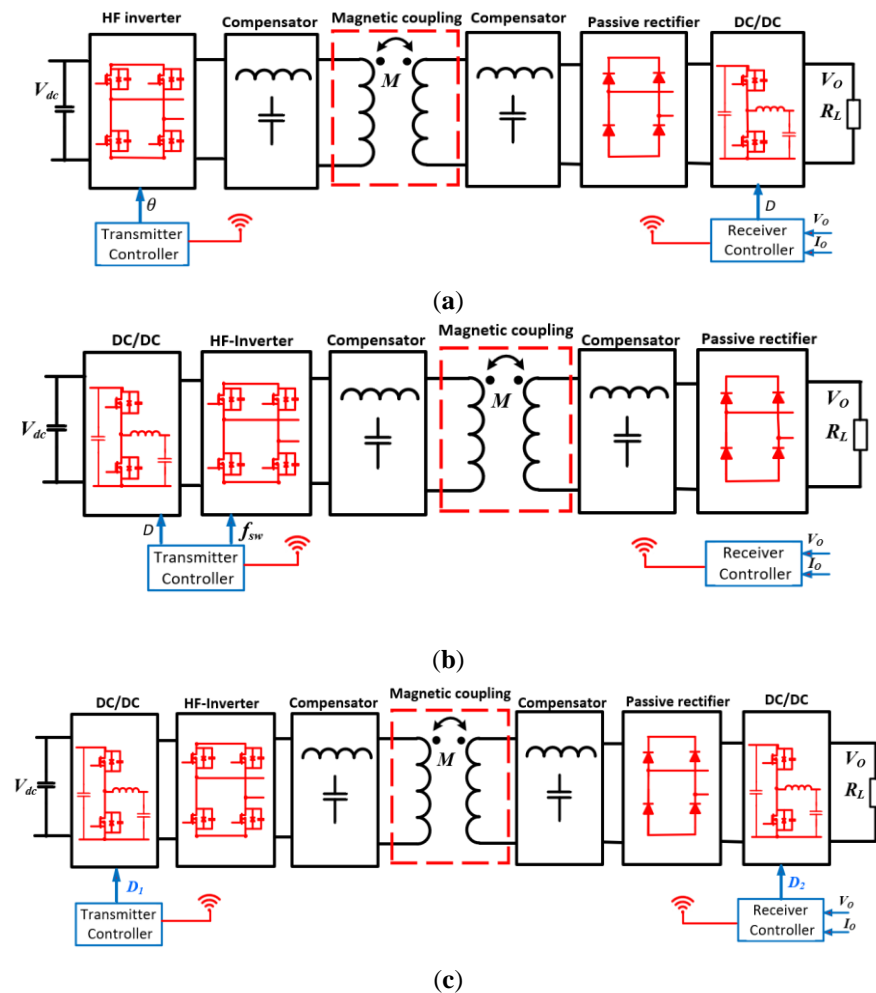

(a)

(b)

(c)

Figure 12. PE structure with auxiliary DC-DC converter: (**a**) with the dc-dc converter on the secondary side, (**b**) dc-dc converter on the primary side, and (**c**) dc-dc converters on both sides.

In Figure 12a, a back-end dc-dc converter is cascaded with a passive rectifier. By adjusting the duty cycle of the converter and phase shift angle of the HF inverter, the equivalent load impedance is varied to track high operation efficiency and output current/voltage control under the misalignment condition or the variation of air gap distance [106–108].

As shown in Figure 12b, a front-end dc-dc converter on the transmitter side combining frequency modulation in an HF inverter is employed to obtain CC/CV charging under ZVS conditions [105]. The CC/CV and impedance matching can be attained simultaneously by two dc-dc converters as in Figure 12c [109–111]. The transmitter side dc-dc converter regulates dc bus voltage for voltage/current regulation while the secondary dc-dc converter is used for impedance matching. It is noticed that additional dc-dc converters operate under hard-switching conditions. Therefore, it undoubtedly reduces the efficiency of the whole system. In particular, the power losses become more severe as the dc-dc converter is employed in the receiver side of low-voltage high-current IPT systems.

4.2. Phase Shift Angle Control

In this control method, the output voltage/current or load impedance can be controlled by regulating phase shift angles on the transmitter side of the HF inverter and/or receiver side of the active rectifier (AR) or semi-bridgeless active rectifier (S-BAR). As illustrated in Figure 13, the phase shift control techniques can be adopted on the transmitter side, receiver side, or both sides. The transmitter side phase-shift control circuit diagram is presented in Figure 13a. The information about output voltage and current are estimated from current and voltage on the primary side [99,100]. The benefit of using such control approaches is that CC/CV profiles can be implemented with fewer components by eliminating dc-dc converters and wireless communication links. However, it requires a complex control algorithm and sensing circuits. In Figure 13b, phase shift angle control can be applied to the rectifier, in which a passive diode rectifier is replaced by an AR or S-BAR. In this circuit configuration, a zero-cross detection circuit is required to synchronize the phase angle, while wireless communication is not necessary [101,102].

(a)

(b)

(c)
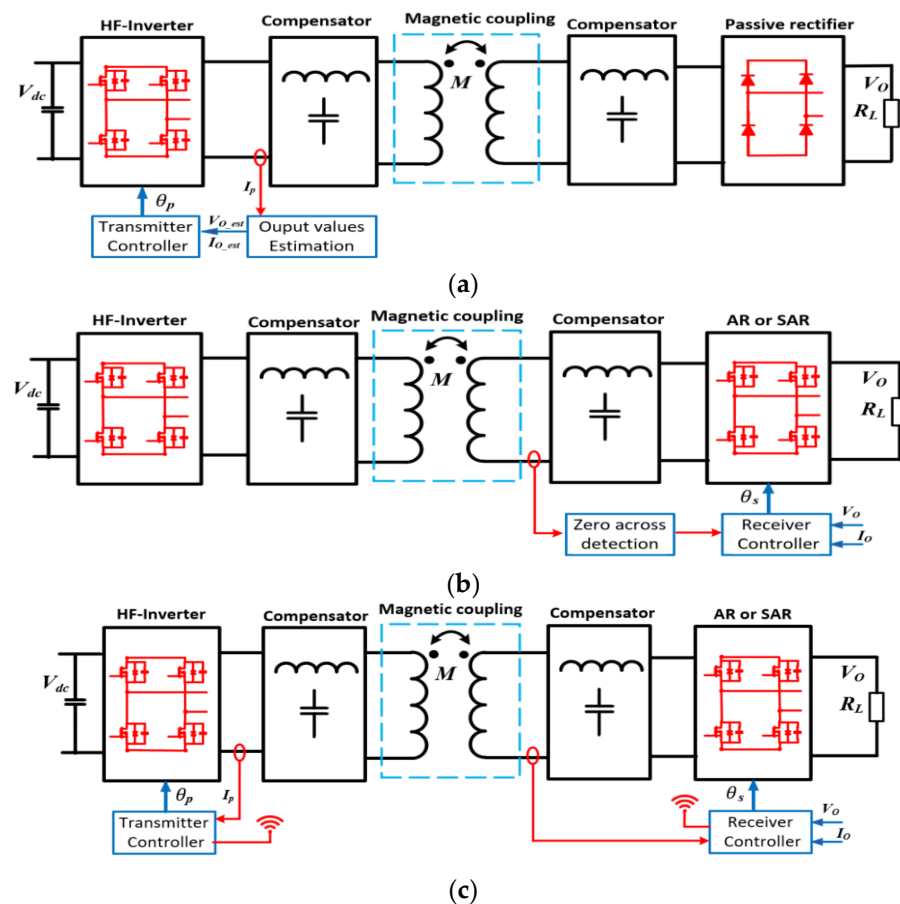
Figure 13. PE structure with phase shift control: (**a**) transmitter side phase shift control, (**b**) receiver-side phase shift control, and (**c**) dual side phase shift control.

In a single-side phase shift control scheme, the desired output current/voltage can be obtained. However, the IPT system may not be operated with maximum efficiency. Therefore dual side phase shift control methods are also widely proposed as demonstrated in Figure 13c. The CC/CV and MET can be obtained simultaneously by adjusting phase shift angles on both sides (θ_P, θ_S) [103,104].

4.3. Frequency Modulation Control

In this frequency control strategy, the variable frequency control is implemented only in the HF inverter, as shown in Figure 14. Based on perturb and observe control with an

estimation algorithm, the maximum efficiency point is tracked by adjusting the switching frequency without a wireless communication link [98]. In [97], the frequency is tuned above the resonant frequency for constant output power and ZVS condition.
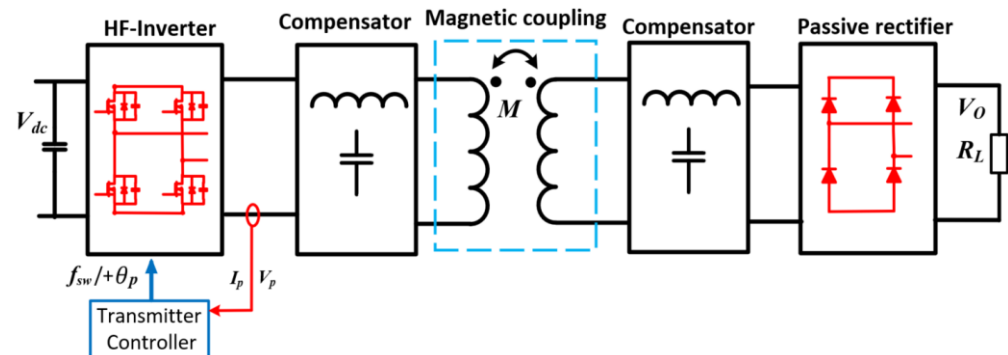

Figure 14. PE structure with frequency control.

This research pointed out that the maximum efficiency under frequency tuning also can be obtained for strong coupling coil systems such as AGV applications. Due to a lack of control degree, the CC/CV implementation cannot be realized by only frequency modulation. To extend the output regulation capability, a combination control method of frequency and phase shift modulation is proposed for CC/CV charging under the ZVS condition [99].

4.4. Reconfigurable Hybrid Compensation

As mentioned and discussed in Section 3.3, load-independent and ZPA characteristics of resonant topologies are used to realize the CC/CV charging profile by switching between two feasible topologies [92–96]. The reconfigurable compensation networks can be located on the transmitter or secondary side as shown in Figure 15. The advantages of this control strategies are that CC/CV charging can be implemented at the fixed resonant frequency and phase shift value. Thus, the IPT system operates at optimal efficiency point, ZPA, and ZVS conditions under a wide range of loads. In addition, there is no feedback closed loop controller. Therefore, this control technique and circuit structure can also be suitable in multi-MHz IPT applications [80]. As compared with the circuit structure in Figure 15a, there is no communication link required as the reconfigurable circuit on the pickup side as in Figure 15b. In this control method, the major drawbacks are that CC/CV charging specifications need to be pre-defined and heavily dependent on coupling inductance and resonant parameters. Hence, it leads to output variation as misalignment happens. In order to implement CV and improve misalignment tolerance, Y. Chen et al. [88] proposed a hybrid reconfigurable topology in which S-LLC and LCC-S topologies are connected with input parallel and output in series configurations. The CC is realized by cascading T-type LCL network as Figure 16. However, it leads to very highly complex circuitry and bulky components.
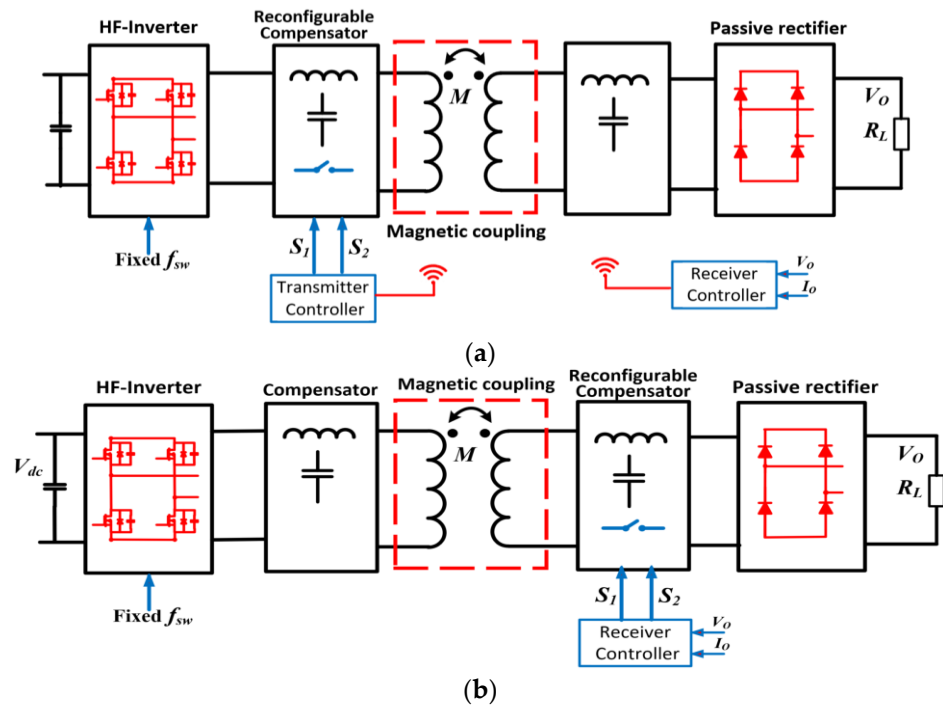
(**a**)

(**b**)

Figure 15. PE structure of reconfigurable hybrid topologies: (**a**) reconfigurable resonant networks on the transmitter side; (**b**) reconfigurable resonant networks on the receiver side.
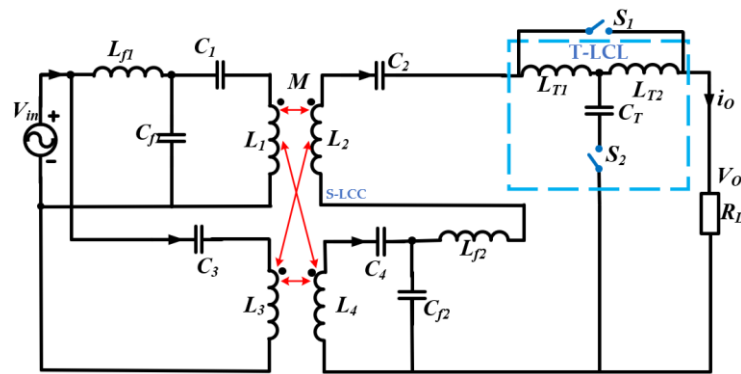

Figure 16. Hybrid and reconfigurable topology with misalignment tolerance [96].

In hybrid resonant topologies, the bidirectional AC switches (ACSs) are widely used to transform from CC topology to CV topology. As depicted in Figure 17, the ACS typically consists of two N-channel MOSFETs connected back to back with each other and triggered by the optically isolated drivers [79].
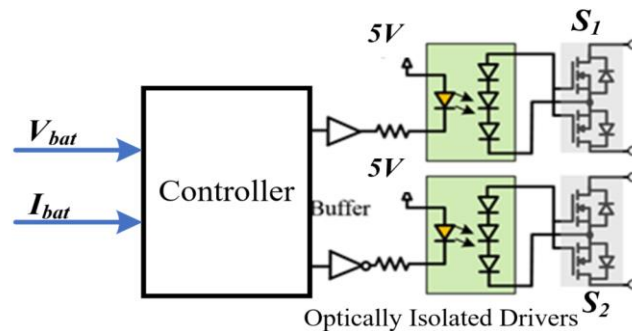
Figure 17. Bidirectional AC switch driving circuit.

4.5. Switchable Dual Frequency

Compared to the methods of hybrid reconfiguration topology, switchable dual-band frequency control methods can implement CC/CV under ZPA conditions with less resonant components and without additional AC switches. It is inspired by the fact that some specific high-order resonant networks possess the characteristics of load independence and ZPA at two different resonant frequencies f_{CC} and f_{CV}. Switchable dual-frequency control methods based on LCC-LCC and LCC-S compensation topologies are proposed in [89,90,112]. The number of components can be reduced further by adopting the S-SP topology [73]. In this control method, a wireless communication link is a must, and controllers are always located on the transmitter side as depicted in Figure 18. As same as the reconfigurable compensation method, the major disadvantage of this control method is output fluctuation under misalignment conditions.
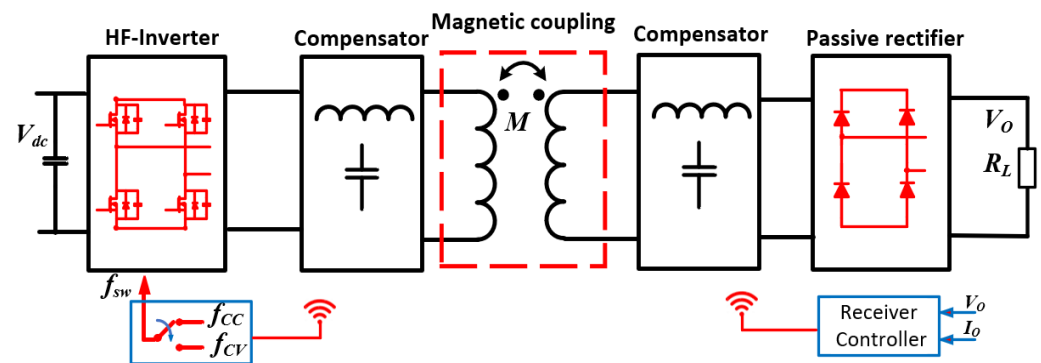
Figure 18. PE structure of switchable dual-frequency control.

4.6. Tunable Compensation Networks

This control method allows for the tuning of a resonant network's impedance under various coupling conditions by adjusting the capacitance and/or inductance values in compensation topologies. As a result, the MET or output regulation can be achieved regardless of misalignment conditions. The tunable resonant components can be capacitors, inductors, or both inductors and capacitors as depicted in Figure 19a. To change the equivalent capacitance, the switchable capacitor array is introduced as in [120,121]. However, this method requires even more active switches and discrete capacitance for tuning. In order to provide continuous capacitance adjustment and reduce component count, switched-controlled capacitors (SCCs) are widely adopted as in [113,117–119]. The circuit structure of SCC is described in Figure 19b. An AC bidirectional switch (ACS) is connected in parallel with a fixed capacitor. The equivalent capacitance value can be tuned by regulating the duty cycles of the ACS driving signal. However, the SCC method leads to additional power losses due to PWM modulation of ACS and requires accurate synchronization of driving signals. As same as a variable capacitor, the variable inductor can be also adopted to provide an additional degree of freedom. By injecting a bias DC into the magnetic core, magnetic permeability is changed. As a result, the effective magnetic reluctance and inductance value are adjustable. The most common variable inductor structure using a double E core is depicted in Figure 19c and applied in both resonant converters and IPT applications [114,115].

Compared to reconfigurable compensation and switchable dual-band frequency, the tunable compensation method requires more complex measurement circuits and control strategies.
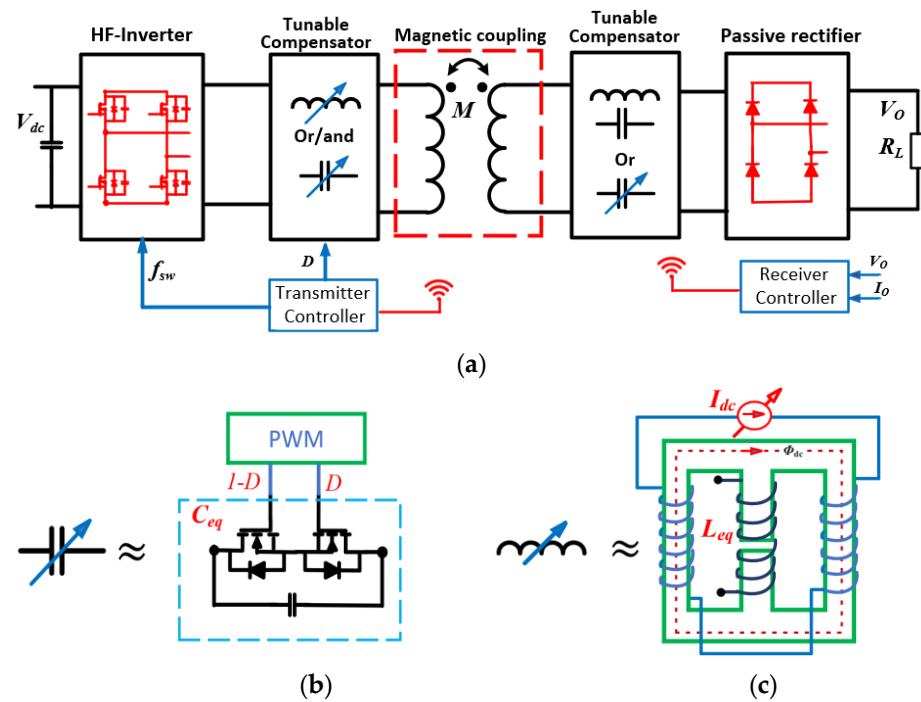
Figure 19. PE structure of tunable compensation networks: (**a**) general PE structure, (**b**) typical tunable capacitor circuit, (**c**) typical tunable inductor circuit.

5. Discussion on Low-Voltage and High-Current IPT Designs

As aforementioned in Section 1 of this paper, low-voltage electric vehicles such as light electric vehicles (LEVs) and Automated Guided Vehicles (AGVs) are rapidly widespread in urbanized and logistics transportation. However, compared to IPT for high-voltage electric vehicles, there is still much less research work on IPT for low-voltage E-mobility applications. As an IPT system is used to charge an LEV or AGV, it encounters additional challenges as identified in Table 6.

Table 6. Design challenges of low-voltage and high-current vehicles.

	LEVs	AGVs
Coupling coefficient k	Loosely coupling < 0.5	Tight coupling > 0.8
Design challenges		
High-current stress on rectifier devices	✓	✓
Large power losses on the receiver side	✓	✓
Require compact design	✓	✓
Sensitive to the air gap variation		✓
High-order harmonic current		✓

As presented in Table 6, low-voltage and high-current IPT systems for AGV applications introduce more difficulties in designing due to tightly coupling, resulting in sensitive output current/voltage and high-order harmonic current. Several solutions have been investigated for both LEVs and AGV applications. However, there is no single solution that can address all issues that arise in low-voltage/high-current IPT systems. This section provides a review of different design considerations regarding coil structures, compensation topologies, and power electronic architectures, which are most suitable for different scenarios. As discussed in Section 2, among the most popular coil configurations, the unipolar circular coil structure has the lowest equivalent series resistance ESRs value. As a result,

it is widely employed as a receiver coil in a wide range of AGVs/LEVs applications with limited receiver installation space [122–124]. However, it is suffered from high RMS current stress on the receiver coil and rectifier switches. In [94], multiple turns parallel Litz-wire is used to handle high-current stress of a 24 V-75 A IPT system. This design technically increases the weight and cost on the receiver side. To address high-current stress issues, dual coil receivers using BP coil configuration are also a suitable candidate [125,126]. In the contrast, the DD coil structure is not suitable to employ in the high-current receiver side due to the large ESRs value. However, it commonly is used on the transmitter side. Selecting a suitable compensation network is also critical to deal with the abovementioned issues. SS resonant topology is among the suitable solutions for low-voltage and high-current IPT systems due to its simple structure, and less component count. Additionally, it is less affected by airgap variation since it operates as a current source. High-order harmonic current and limited design flexibility are obstacles to the SS topology [122,124,127]. LCC-LCC resonant topology can offer current source characteristics as same as the SS compensator. In addition, LCC-LCC topology owns two advantages over SS topology in terms of degrees of freedom in parameter designing and lower high-order harmonic current. Thus, double-side LCC is also considered an attractive solution for low-voltage and high-current IPT systems in both LEVs and AGV applications [123,126,128,129].

Regarding the selection of power electronic architectures, low-voltage and high-current IPT systems can adopt the same structure for the transmitter as in high-voltage IPT systems. However, it needs to be considered high-current stress issue exists on the receiver side. To handle high-current stress on the rectifier circuits, dual rectifiers coming along with dual receiver coils can reduce current stress on receiver coils and rectifier switches as depicted in the circuit diagram in Figure 20 [125,126,128]. In [126], dual synchronous active rectifiers are used for further reducing power losses and output regulation. In addition, Figure 21 shows another solution of secondary topologies, inspired by the current double rectifiers (CDRs) circuit for high current in DC/DC converter applications [130–132].
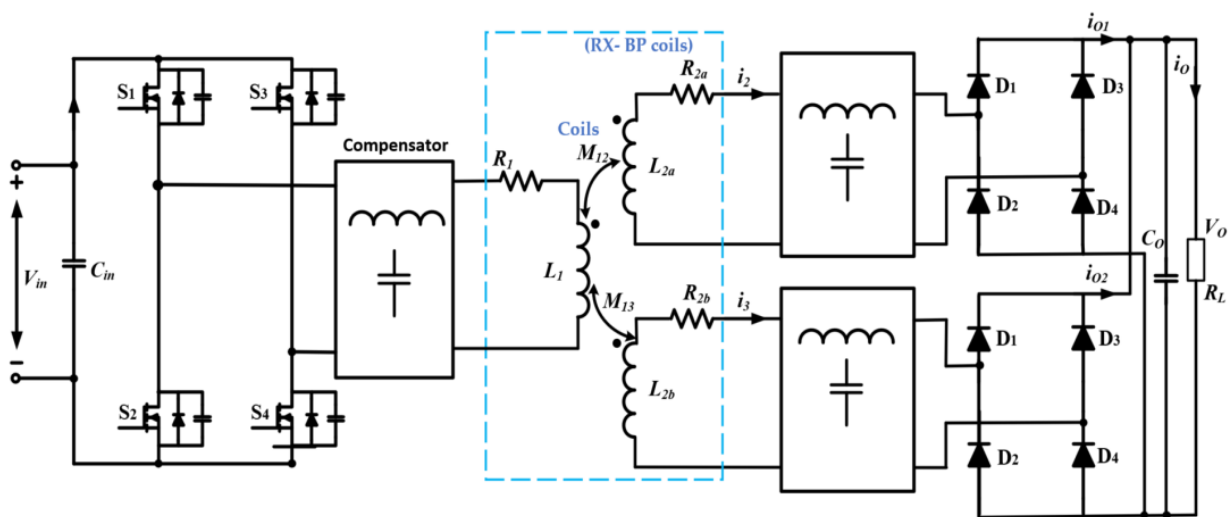

Figure 20. A typical dual-coil and dual-rectifier circuit architecture for a high-current IPT system.

As shown in Figure 21, since the secondary current output is reduced by half of the output current, current double rectifiers and their modifications are used to deal with the high-current stress on rectifiers in high-current IPT systems [127,133–135]. In [127], a 10 kW 400 V/48 V IPT is proposed with an ICCDR structure to handle 200 A output current and achieves an overall efficiency of 94%. As summarized in Table 7, several studies on low-voltage/high-current IPT systems have been introduced in recent years.
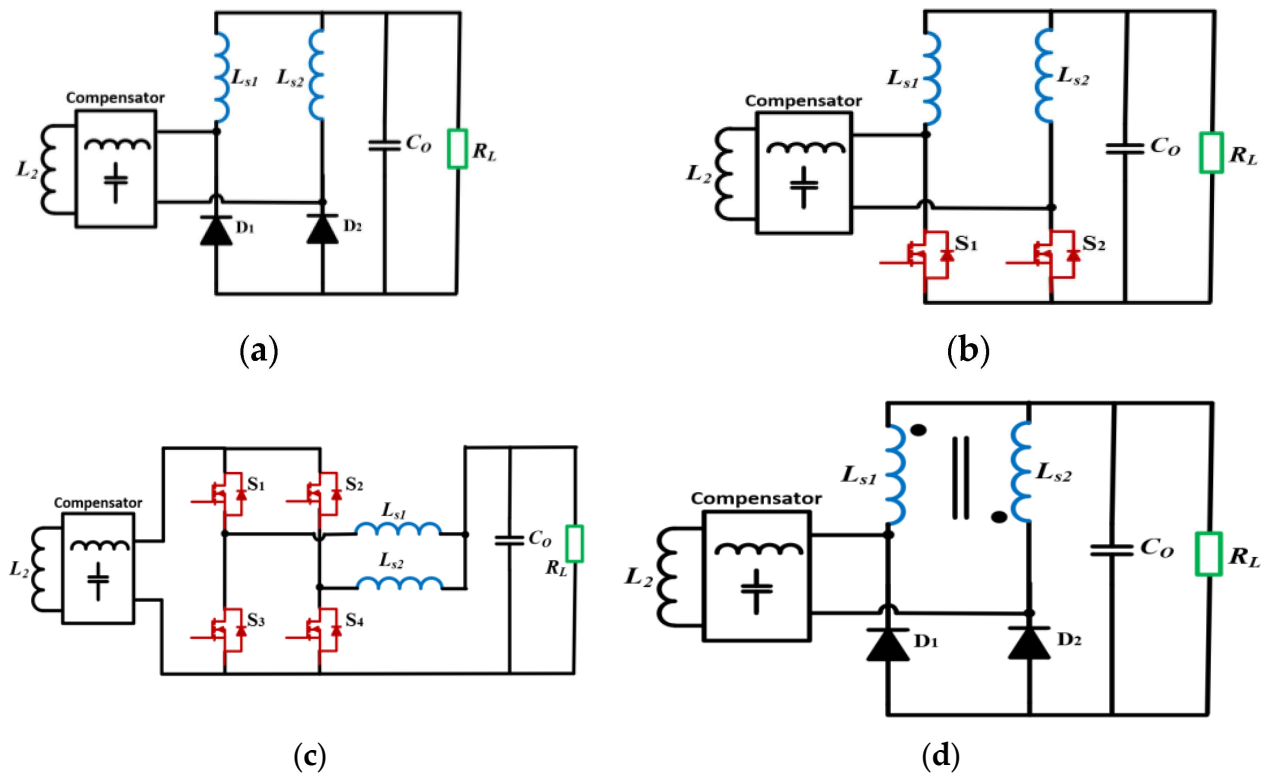
Figure 21. Secondary circuit diagrams of IPT system based on current double rectifiers CDR. (**a**) Conventional CDR [133]. (**b**) CDR with active switches [134], (**c**) current double synchronous rectifier CDSR [135] and (**d**) inverse coupled current double rectifier ICCDR [127].

Table 7. Recent studies on wireless power transfer systems for low-voltage and high-current applications.

Ref. /Years	Applications	Coil Structures-TX/RX and Dimension	Resonant Topologies	Vin, P_O, V_O, I_O,	Coupling k, f_{sw}, Efficiency	Circuit Structures and Design Objectives
[123] 2019	AGV	• Rectangular/rectangular • 220 × 200 × 10 mm • Airgap: 15 mm	LCC-LCC	• 300 V/1.8 kW • 24 V/75 A	• 0.8, • 85 kHz, • 86.1%,	• FB/Diode rectifier • reduce harmonic
[124] 2019	AGV	• Rectangular/rectangular • 220 × 220 × 10 mm • Airgap: 10 mm	SS	• 400 V/1.8 kW • 24 V/75 A	• 0.7, • 85 kHz, • 86.1%,	• FB/Diode rectifier • reduce harmonic
[126] 2022	LEV	• Rectangular/BP • 200 × 160 × 25 mm • Airgap: 30 mm	LCC-LCC	• 350 V/1.2 kW • 24 V/50 A	• 0.35, • 200 kHz, • 92%,	• FB/Dual active rectifiers • MET (secondary phase shift control)
[136] 2020	LEV	• Circular/circular • 320 mm • Airgap: 105 mm	LCL-S	• 400 V/300 W • 48 V/7 A	• 0.24, • 200 kHz, • 91.7%	• FB/Diode rectifier • Output voltage regulation (primary phase shift control)
[122] 2022	AGV	• Circular/circular • 320 mm • Airgap: 40 mm	SS	• 400 V/2.5 kW • 48 V/50 A	• 0.63, • 100 kHz, • 93.5%	• FB/active rectifier • MET (frequency tuning)
[127] 2022	LEV, AGV	• Rectangular/rectangular • 310 × 316 mm • Airgap: 40 mm	SS	• 400 V/10 kW • 48 V/200 A	• 0.4 • 100 kHz, • 94%	• FB/Inverse coupled Current double rectifier (ICCDR)
[135] 2022	LEV, AGV	• Circular/circular • N/A • Airgap: 50 mm	LCC-P	• 48 V/1 kW • 24 V/40 A	• 0.51 • 85 kHz, • 87.4%	• Quasi-Z source inverter/current-double synchronous rectifier (CDSR) • Constant power, MET
[137] 2022	AGV	• Circular/circular • N/A • Airgap: 70 mm	LCC-LCC	• NA/700 W • 72 V/10 A	• 0.4 • 85 kHz, • 91%	• FB/Diode rectifier • Output voltage regulation, minimize current stress on the secondary coil (tunable capacitor using SCC)
[138] 2022	AGV	• Rectangular/rectangular • TX coil: 300 × 1500 mm, • RX coil: 300 × 300 mm • Airgap: 30~90 mm	T-type/Series(T/S)	• 200 V/1 kW • 50 V/20 A	• 0.28~0.13 • 85 kHz, • 85%	• FB/Diode rectifier • Design method of T/S compensation for maintaining stable output current

6. Design Example for Low-Voltage and High-Current IPT Applications

In previous review sections, the current trends and challenges of general IPT as well as low-voltage/high-current IPT applications have been comprehensively reviewed and identified by considering several design aspects including coils, compensation topologies, and power electronic architecture selections. To deal with high-current stress and current imbalance under misalignment and component tolerance conditions, an asymmetric LCC-LCC compensator and DD-BP coil structure with a passive current-sharing method are proposed in this paper. The proposed circuit architecture is depicted in Figure 22, in which

two separated capacitors and inductors in dual compensator circuits are connected in parallel to form a common capacitor and common inductor circuit structure.
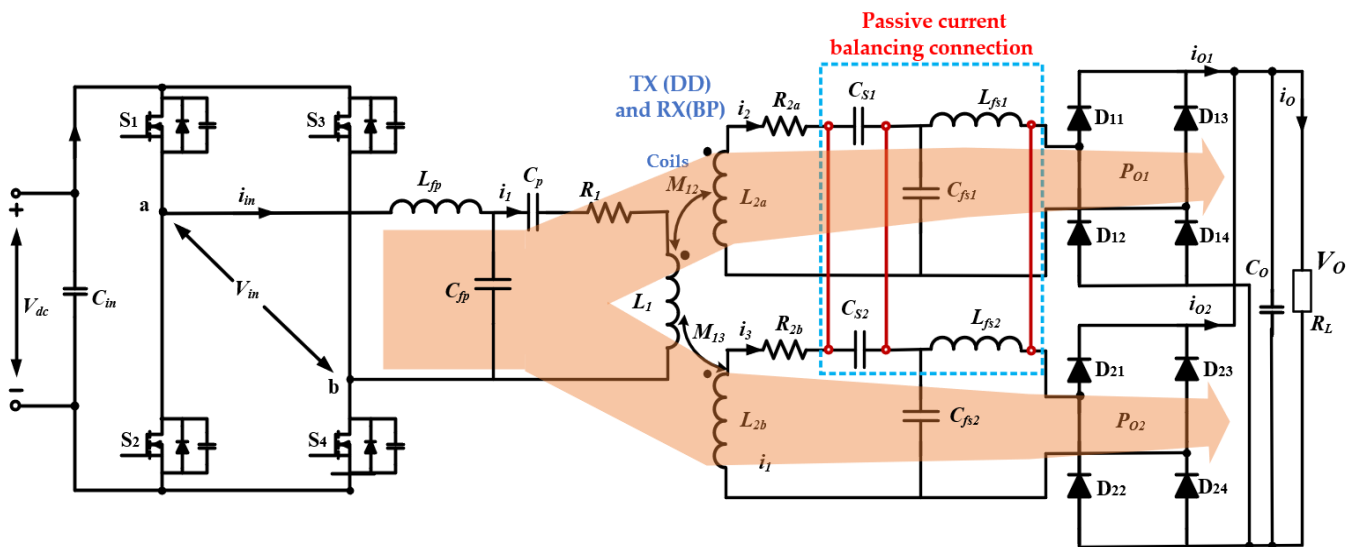

Figure 22. Proposed IPT system for LEV applications.

This current-sharing method is inspired by the concept of a common capacitor and common inductor multiphase LLC resonant converter [139,140]. Thereby, the current information of each phase is extracted and shared automatically without applying active control methods. Since high RMS current passes through L_{fs}, symmetric resonant parameters of LCC-LCC with $L_{fp} = L_{fs}$, $L_1 = L_2$ results in a larger conduction loss in receiver side [128]. In the proposed design, asymmetric resonant compensation components are proposed to reduce RMS current in the receiver coil and compensation components. As a case study, Table 8 contains the design specifications for the 2.5 kW-48 V IPT. And the design method of compensation parameters is presented in Section VI.B.

Table 8. Design specification of proposed IPT for LEV applications.

Parameters	Symbols	Values
Input voltage	V_{dc}	400 V
Output voltage	V_O	48 V
Output Power	P_O	2500 W
Switching frequency	f_O	85 kHz

6.1. Coils Design

In this design, DD and BP coils structures with ferrite rods are selected for TX and RX, as shown in Figure 23a. The coil dimension of 400 × 400 mm is implemented for LEVs and The mutual inductance between the DD and BP coils are simulated at a 100 mm transfer distance which is suitable for LEVs applications. When designing a BP coil, the critical task is to decouple mutual inductance between L_{2a} and L_{2b} the coils while maintaining the desired outer dimensions. Ansys Maxwell software is used to estimate all magnetic parameters and the overlap distance of the BP coil structure for decoupling as depicted in Figure 23b,c. As resulting from simulation, the design coil parameters are listed in Table 9.
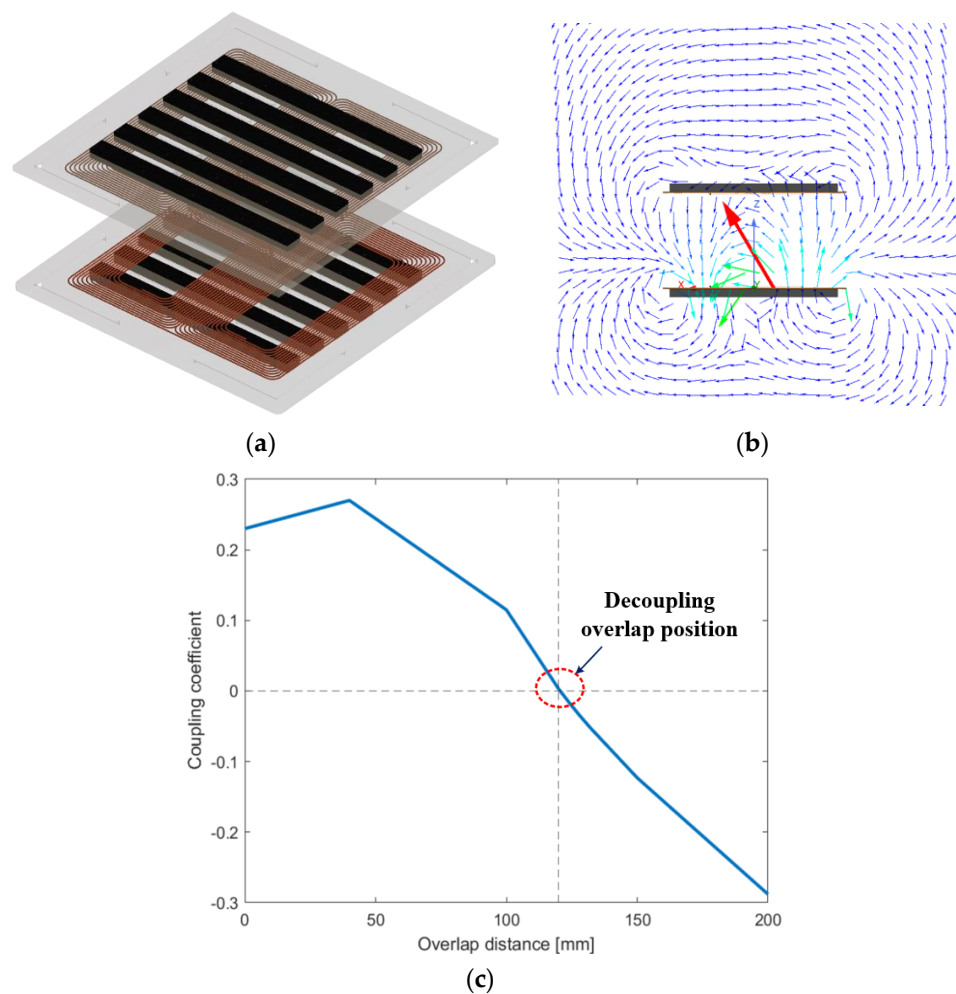
Figure 23. Coils design and simulation: (**a**) a 3D model of coil system, (**b**) flux path of DD-BP coils, and (**c**) estimated decoupling overlap position by simulation.

Table 9. Design specifications of coil prototype.

Parameters	Value
Coils dimension	400×400 mm
TX-DD coil L_1	235 uH
RX-BP coil L_{2a}, L_{2b}	116 uH
Mutual inductance M_{12}, M_{13}	56 uH
Overlap distance BP coil	121 mm
Air gap distance	100 mm
Ferrite bar pitch	26 mm
Ferrite bar material	N87
Litz wire	AWG38 $\times$ 300 strands

6.2. Proposed Asymmetric LCC-LCC Compensation Network

In this design, the BP receiver coil and LCC-LCC compensation topology are selected for a low-voltage and high-current IPT system due to power-sharing capability, high degree of freedom, high misalignment tolerance, and low order harmonic current. The equivalent circuit is illustrated in Figure 24. The AC circuit of LCC-LCC is analyzed by using the fundamental harmonic approximation (FHA). To simplify the analysis, all parasitic

resistances are eliminated, and the output current gain equation I_{O1}/V_{in} or I_{O2}/V_{in} can be derived separately based on the superposition theorem. Table 10 provides a summary of the calculations of the LCC-LCC AC equivalent model. The calculations based on the AC equivalent model of LCC-LCC are briefly listed in Table 10. To reduce the high ESR value of receiver compensation inductors L_{fs1} and L_{fs2}, the inductance values of L_{fs1}, L_{fs2} should be designed as small as possible to handle high RMS current. From Equations (11) and (12) in the Table 10, the ratio between the transmitter coil current and receiver coil current is established to be equal unity as (13).

Table 10. Analysis of LCC-LCC compensation topology.

DC and AC Conversion		Defined receiver equivalent impedances	
$\begin{cases} V_{in} = \frac{2\sqrt{2}V_{dc}}{\pi}; V_O = \frac{2\sqrt{2}V_b}{\pi} \\ R_{ac1} = R_{ac2} = \frac{8(2R_O)}{\pi^2} \\ i_{O1} = i_{O2} = \frac{\pi}{2\sqrt{2}(I_b/2)} \end{cases}$	(5)	$\begin{cases} Z_{eq1} = \frac{1/(j\omega C_{eq})(R_{ac1}+j\omega L_{fs1})}{1/(j\omega C_{eq}+R_{ac1}+j\omega L_{fs1})} \\ Z_{S1} = j\omega L_{2a} + \frac{1}{j\omega C_{s1}} + Z_{eq1} \end{cases}$	(6)
Defined transmitter equivalent impedances		**Transmitter and receiver currents**	
$\begin{cases} Z_{ref1} = \frac{\omega^2 M_1{}^2}{Z_{S1}} \\ Z_{p1} = j\omega L_1 + \frac{1}{j\omega C_1} + Z_{ref1} \\ Z_{p2} = \frac{1/(j\omega C_{fp})Z_{p1}}{1/(j\omega C_{fp})+Z_{p1}} \\ Z_{in1} = j\omega L_{fp} + Z_{p2} \end{cases}$	(7)	$\begin{cases} I_{in} = \frac{V_{in}}{Z_{in}}; I_1 = \frac{I_{in}Z_{p2}}{Z_{p1}} \\ I_2 = \frac{j\omega M_1 I_1}{Z_{S1}}; I_{01} = \frac{Z_{eq1}I_2}{R_{ac1}+j\omega L_{fs1}} \end{cases}$	(8)
The current gain equation		**Resonant conditions to obtain load-independent current and ZPA**	
$G_{IV1} = \frac{I_{01}}{V_{in}} = \frac{Z_{eq1}j\omega M_1 Z_{p2}}{(R_{ac1}+j\omega L_{fs1})Z_{S1}Z_{p1}Z_{in}}$	(9)	$\begin{cases} C_P = \left(\omega_0{}^2\left(L_1 - L_{fp}\right)\right)^{-1} \\ C_{S1} = \left(\omega_0{}^2\left(L_{2a} - L_{fs1}\right)\right)^{-1} \\ C_{S2} = \left(\omega_0{}^2\left(L_{2b} - L_{fs2}\right)\right)^{-1} \\ C_{fp} = \left(\omega_0{}^2 L_{fp}\right)^{-1} \\ C_{fs1} = \left(\omega_0{}^2 L_{fs1}\right)^{-1} \\ C_{fs2} = \left(\omega_0{}^2 L_{fs2}\right)^{-1} \end{cases}$	(10)
Transmitter and receiver currents at the resonant frequency ω_0		Similarly for the second receiver coil side, the coil current $\boldsymbol{i_3}$, output current $\boldsymbol{I_{O2}}$ and total output current $\boldsymbol{i_O}$	
$\begin{cases} i_{in} = \frac{M_1 V_{in}}{j\omega_0 L_{fp}L_{fs1}} \ i_1 = \frac{V_{in}}{j\omega_0 L_{fp}} \\ i_{O1} = \frac{M_1 V_O}{j\omega_0 L_{fp}L_{fs1}} \ i_2 = \frac{V_O}{j\omega_0 L_{fs1}} \end{cases}$	(11)	$I_3 = \frac{V_O}{j\omega_0 L_{fs2}}; i_{O2} = \frac{M_2 V_O}{j\omega_0 L_{fp}L_{fs2}}$ $i_O = i_{O1} + i_{O2}$	(12)

$$\frac{I_1}{I_2} = \frac{I_1}{I_3} = \frac{V_{in}}{V_O}\frac{L_{fs1}}{L_{fp}} = \frac{V_{in}}{V_O}\frac{L_{fs2}}{L_{fp}} = 1 \tag{13}$$
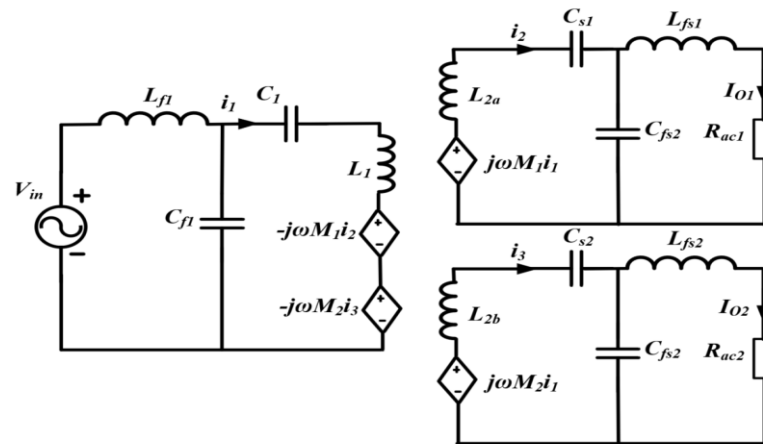
Figure 24. Equivalent decoupled circuit model of LCC-LCC compensation of the primary side (DD) and the secondary side (BP).

As a result, the receiver coil RMS currents can be selected the same as in transmitter coil RMS current, resulting in the inductance value L_{fs1} is smaller than L_{fp} by a proportion of V_{in}/V_O. Therefore, the parasitic resistance ESR value of L_{fs1}, L_{fs2}, is reduced.

$$\frac{L_{fs1}}{L_{fp}} = \frac{L_{fs2}}{L_{fp}} = \frac{V_O}{V_{in}} \tag{14}$$

Substituting (14) into (11) and (12), the inductance values of L_{fp}, L_{fs1}, and L_{fs2} of LCC-LCC compensation can be derived as:

$$L_{fp} = \sqrt{L_{fp}L_{fs1}V_{in}/V_O}$$
$$L_{fs1} = L_{fs2} = \sqrt{L_{fp}L_{fs1}V_O/V_{in}} \tag{15}$$

The values of compensation capacitors are calculated as in (10). The compensation parameters of the proposed design method are listed in Table 11.

Table 11. Compensation parameters for 48 V IPT system.

Parameters	Values
C_P	27.32 nF
C_{fp}	32.85 nF
L_{fp}	106 uH
L_{fs1}, L_{fs2}	12.8 uH
C_{fs1}, C_{fs2}	273.8 nF
C_{s1}, C_{s2}	36.1 nF

6.3. Proposed Passive Current Sharing Method of LCC-LCC—BP Receiver Coil

In this sub-section, the basic concept of the proposed passive current-sharing technique for the BP receiver coil is briefly presented. The BP receiver coil structure is considered to have high misalignment tolerance [45]. However, this coil structure still has the problem of current imbalance between receiver coils and rectifier circuits due to the tolerance of resonant components and coils misalignment. As a result, one coil and rectifier operate at high-current stress while others are in light load condition. This issue is exacerbated in low-voltage and high-current applications since a minor component parameter mismatch can result in a significant current imbalance among receiver coils. In this paper, the passive

balancing solution, so-called passive impedance matching is proposed for double-side LCC topology with a BP receiver.

By connecting C_{S1} to C_{S2} and L_{fs1} to L_{fs2} in parallel, the equivalent model of LCC-BP receiver coil with common-capacitor and common- inductor connection is depicted in Figure 25. Under misalignment and component mismatch conditions, $M_1 \neq M_2$, $L_{2a} \neq L_{2a}$, $C_{1s} \neq C_{2s}$, $C_{fs1} \neq C_{fs2}$ or $L_{fs1} \neq L_{fs2}$, it results in $i_2 \neq i_3$ and $i_{01} \neq i_{02}$. The simplified model and the phasor diagram without the current balancing technique are illustrated in Figure 26a, where the impedances of Z_{eq1}, Z_{eq2} are defined as in Equation (16). It can be seen that current i_2 and i_3 can be different in magnitude and phase angle due to both misalignment and component tolerances problems. A small mismatch may cause the deviation of current stress in each coil L_{2a}, L_{2b} and rectifiers.

$$\begin{cases} Z_{eq1} = \frac{j\omega L_{fs1} R_{ac1}}{j\omega L_{fs1} + R_{ac1}} \\ Z_{eq2} = \frac{j\omega L_{fs2} R_{ac2}}{j\omega L_{fs2} + R_{ac2}} \\ Z_{Cs1} = (j\omega C_{s1})^{-1} \\ Z_{Cs2} = (j\omega C_{s2})^{-1} \end{cases} \tag{16}$$
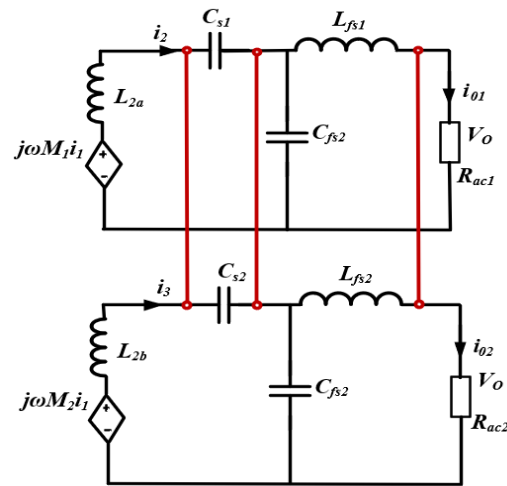

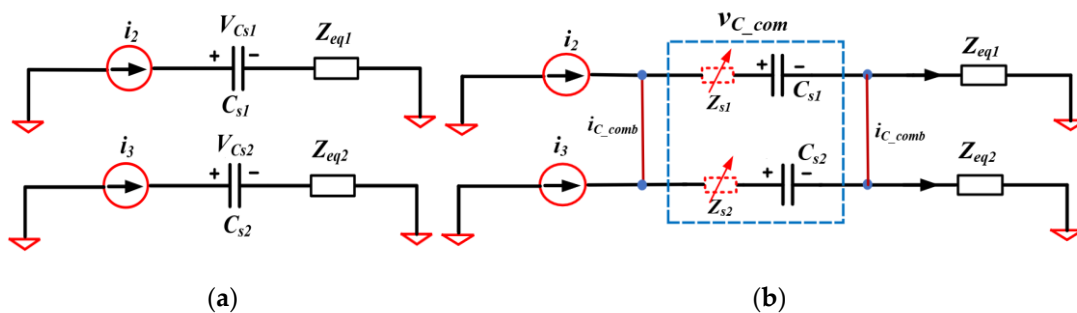**Figure 25.** AC equivalent circuit of LCC-LCC BP receiver with passive balancing configuration.

(a)

(b)

Figure 26. Equivalent circuit of capacitors in LCC-BP receiver coils (**a**) without common capacitor connection, and (**b**) with common capacitor connection.

By paralleling capacitors C_{S1}, C_{S2}, a common capacitor C_{com} and two virtual impedances Z_{s1}, and Z_{s2}, are created as illustrated in Figure 26b. Assuming that α, β are phase different

angles of i_2 and i_3 referred to common capacitor current i_{C_com} due to components tolerance and misalignment. The new circuit model is expressed by (17).

$$\begin{cases} i_2 = I_2 e^{j\alpha} \\ i_3 = I_3 e^{j\beta} \\ i_{C\_com} = i_2 + i_3 \\ V_{C\_com} = i_2 Z_{s1} + i_2 Z_{Cs1} = i_3 Z_{s2} + i_3 Z_{Cs2} \end{cases} \tag{17}$$

As illustrated in Figure 27, the phasor diagrams of the circuit model are represented with an assumption that the current i_2 is leading while current i_3 is lagging to i_{C_com} by the phase angle of α and β, respectively. It can be observed that two virtual impedances Z_{s1} and Z_{s2} are automatically formed to satisfy Equation (17). In addition, the virtual impedance Z_{s1} and Z_{s1} can be negative and positive resistance to prevent the current i_3 from increasing and i_2 form decreasing.
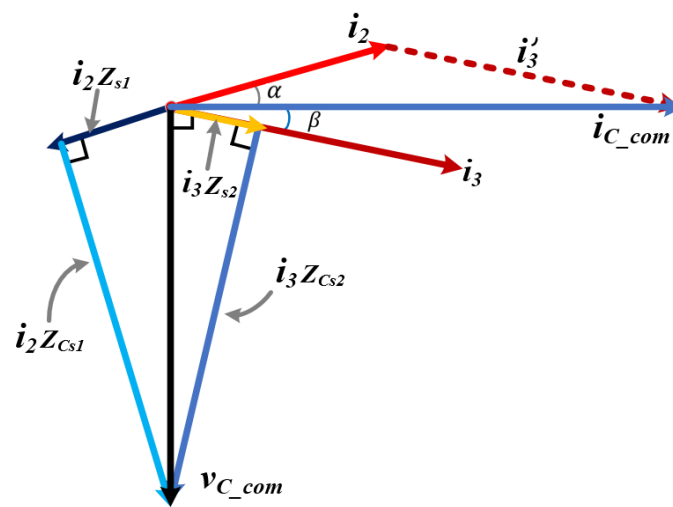

Figure 27. The phasor diagrams of equivalent circuit models with common capacitor connection.

Similarly, the passive impedance matching technique can be also applied to the resonant inductors L_{fs1} and L_{fs2} for further enhancing current balance capability. Figure 28a shows the equivalent circuit of two inductors without parallel connection and with parallel connection. The current i_{o1}, i_{o2}, flowing through L_{fs1} and L_{fs2}, are assumed to have a difference in phase and magnitude as defined as Equation (18)

$$\begin{cases} i_{01} = I_{01} e^{j\gamma} \\ i_{02} = I_{02} e^{j\theta} \\ Z_{Lfs1} = j\omega L_{fs1} \\ Z_{Lfs2} = j\omega L_{fs2} \\ V_{Lfs1} = i_{01} Z_{Lfs1} \neq V_{Lfs2} = i_{02} Z_{Lfs2} \end{cases} \tag{18}$$

where V_{Lfs1}, V_{Lfs2} are the voltage across L_{fs1} and L_{fs2}, respectively. As same as common capacitor connection, the common inductor is formed by paralleling two inductors L_{fs1}, L_{fs2}. The equivalent circuit is illustrated in Figure 28b and expressed as Equation (19)

$$\begin{cases} i_{L\_com} = i_{01} + i_{02} \\ v_{L\_com} = i_{01} Z_{fs1} + i_{01} Z_{Lfs1} \\ \quad = i_{02} Z_{fs2} + i_{02} Z_{Lfs2} \end{cases} \tag{19}$$
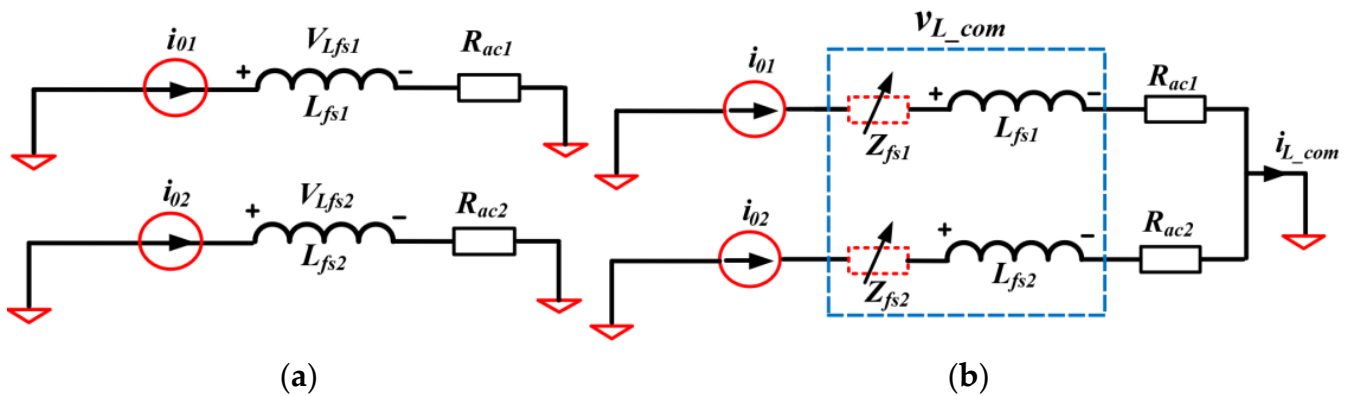
Figure 28. Equivalent circuit of inductors in LCC-BP receiver coils (**a**) without common inductor connection, and (**b**) with common inductor connection.

The phasor diagram of Equation (19) can be demonstrated in Figure 29, where the reference vector i_{L_com} is the sum of two inductor current i_{01} and i_{02}. It can be seen that i_{L_com} is lead by i_{01} and lagged by i_{02} with the phase angle of γ and θ. Moreover, a virtual impedance Z_{fs1} with positive value and Z_{fs1} with negative values are added virtually to satisfy Equation (19). Therefore, current i_{01}, i_{02} are adjusted automatically.
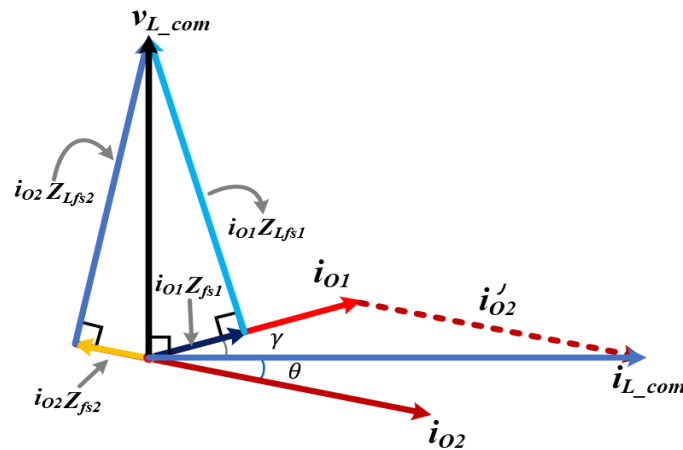

Figure 29. The phasor diagrams of equivalent circuit model with common inductor connection.

By adopting the passive impedance matching technique for capacitors and inductors of LCC-BP receiver coils, the equivalent impedance of the capacitor and inductor are changed. Hence, the current sharing between the dual receiver coils and dual rectifiers can be achieved without any closed-loop control methods.

6.4. Simulation Results

In this section, MATLAB and PSIM software are used to validate the design procedure and effectiveness of the proposed method for a design example of a low-voltage and high-current IPT system. The output current and input impedance phase angle versus frequency are plotted in Figure 30 by using the design parameters in Tables 9 and 11, and the current gain expression in Equation (9). At a resonant frequency of 85 kHz, a constant current of 50 A and ZPA are achieved with different output powers. The output current can be seen to be capable of maintaining a constant value. Nevertheless, the switching frequency should be selected slightly less than the resonant frequency 85 kHz to ensure soft-switching condition. To further verify the proposed design, the key simulation waveforms are provided as shown in Figure 31. The simulation model is set at the ideal condition without considering the misalignment and component tolerances. The primary current and AC input voltage

are totally in phase, meaning no circulating current due to reactive power has been seen in Figure 31.
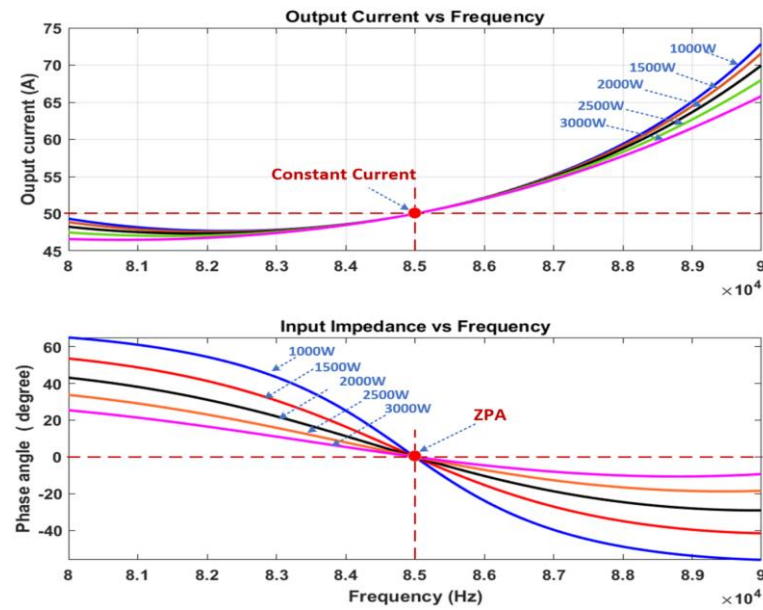

Figure 30. Output current and phase angle versus frequency of proposed IPT design at various output powers.
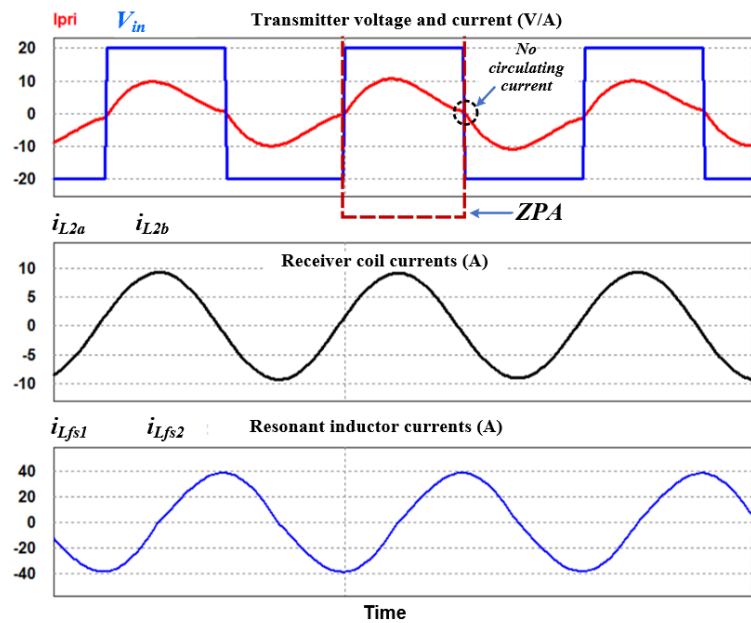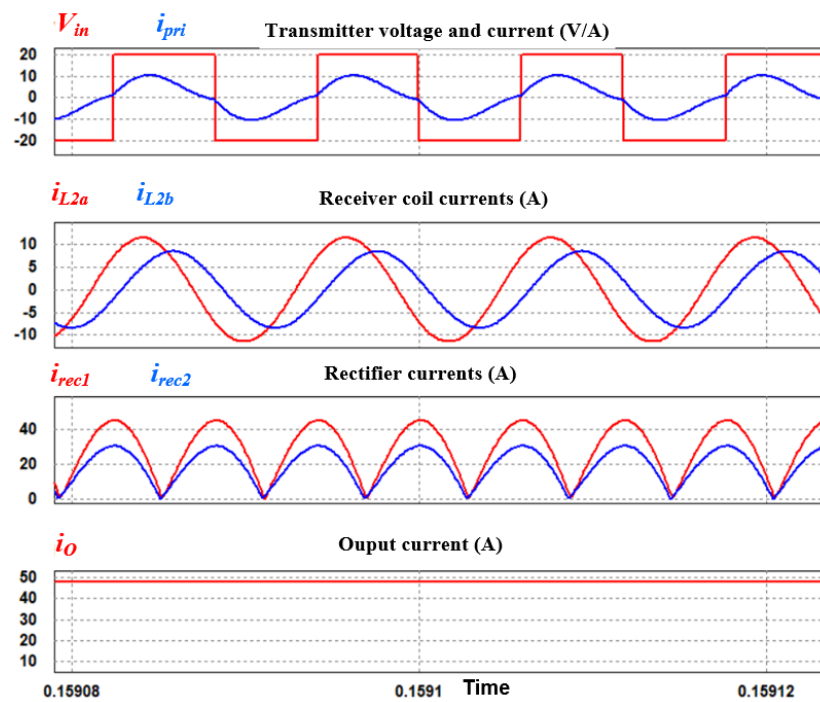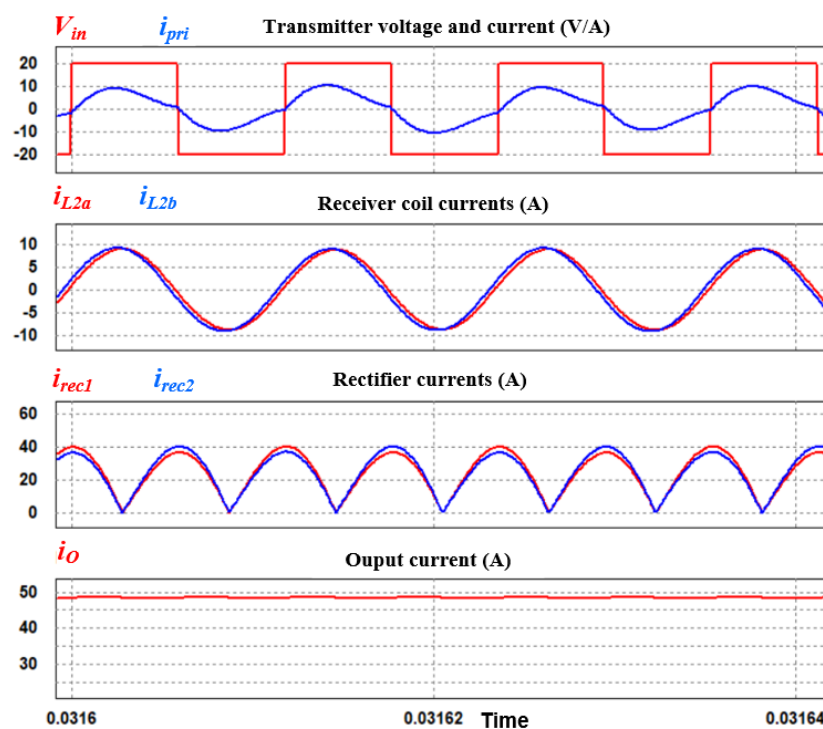

Figure 31. Key simulation waveforms under perfect alignment, zero component tolerance condition.

The RMS current of dual receiver coils i_{L2a}, i_{L2b} are designed to be the same as the RMS current of the transmitter i_{pri}. To validate the effectiveness of passive current balancing solution for LCC-LCC topology with dual coil BP structure. The proposed IPT system is simulated with misalignment and component mismatch conditions by setting $M_1 = 0.73M_2$, $C_{fs2} = 0.95C_{fs1}$, $L_{fs1} = 1.1L_{fs2}$, $C_{s1} = 0.95C_{s2}$. Figure 32a shows the simulation waveform of the proposed IPT design without common capacitor connections. It is clearly observed that the dual receiver coil currents i_{L2a}, i_{L2b} are deviated in both phase and magnitude. In addition, one full-bridge diode rectifier has to handle more current than the other ($i_{rec1} > i_{rec2}$), causing an increase in power losses. The unbalancing current becomes more

server for high-current IPT systems under high misalignment scenarios. As shown in Figure 32b, the deviation of currents in receiver coils and rectifiers is significantly improved.

(**a**)

(**b**)

Figure 32. Key simulation waveforms of proposed IPT under misalignment and component tolerance condition: (**a**) without passive current sharing technique, and (**b**) with passive current sharing technique.

In the proposed 2.5 kW-400 V/48 V-50 A design, the TX and RX coils have the same dimension, Litz wire diameter, and current stress (~7.5 A) on both the high- and low-voltage sides. Furthermore, the passive impedance matching technique allows automatic current sharing in the BP-LCC receiver structure without the need for additional components or closed-loop control. These characteristics distinguish the proposed solution from the other existing designs in Table 7.

7. Discussion and Future Works

High-voltage IPT systems for HV battery vehicles have been a mainstream topic in academic and industrial research for decades. Recently, LEVs and AGVs with low-voltage batteries have gained popularity in the urban transportation and intralogistics sectors. Hence, there is undeniably a growing trend toward the use of wireless charger systems for LEVs and AGV applications in both dynamic and static charging scenarios. This work covered a wide range of aspects, including fundamental theory, coil pad designs, compensation topologies, power electronic architecture, and control methods applicable to both high-voltage and low-voltage stationary IPT systems. Some related subjects are still beyond the scope of this works and suggested to further discuss and investigate in future works as follows:

- For AGV applications, dynamic IPT solutions can be applied to reduce battery size, replace batteries with supercapacitors, or remove batteries entirely. Thus, vehicles can extend their operating time.
- Because of high-current stress on the receiver side. More studies into the circuit topologies, sensing techniques, and control methods of synchronous rectifiers is needed to improve the system's efficiency.
- Wide BandGap (WBG) devices, such as Gallium-Nitride (GaN) semiconductors, can be used in high-frequency IPT for AGV applications, where the frequency can be increased to several hundreds of kHz or MHz to significantly reduce the volume of the coils and passive resonant components. Meanwhile, the frequency band for IPT-LEVs remains limited by the SAE J2954 standard, recommended range of 81 kHz to 90 kHz.

In comparison to previous low-voltage/high-current IPT systems, this paper introduces an asymmetrical LCC-LCC structure to address the problem of high-current stress on receiver sides. In addition, passive current sharing techniques effectively compensate for the current imbalance problem in the BP coil configuration due to mismatched components or misalignment. However, the following future work are required to further validate the benefits of the proposed 2.5 kW IPT system:

- Experiment waveforms should be provided to validate the design concept through the implementation of hardware setups including DD-BP coils, LCC-LCC compensation, and HF-inverter/rectifier.
- Although the proposed IPT design for loosely coupled LEVs applications has the advantage of a very low turn-off switching current as shown in simulation waveforms, the feasibility of the proposed methodology for tightly coupled AGV applications needs to be investigated further in future work.

8. Conclusions

This paper reviewed the current status of stationary IPT systems for low-voltage and high-current electric mobility applications. The key aspects, including coil structure, compensation topologies, control methodologies, and power electronic architectures, were intensively reviewed to provide a review map and design guidelines. Compared to massive previous review works, this paper was the first to review and identify the trends and challenges of low-voltage and high-current IPT systems. After that, a design example approach was proposed to address high-current stress and current imbalance issues in the BP-LCC receiver-side configuration. In this method, the RMS current on the high-voltage transmitter and low-voltage receiver sides had the same value, resulting in less power loss in the receiver coil while keeping the same dimension and wire diameter as the

transmitter coil. In addition, the proposed passive current sharing method significantly improved the current imbalance problem caused by misalignment and component tolerance conditions. The theoretical analysis and simulation results are provided to demonstrate the effectiveness of the proposed design. Future works are also recommended for further investigation, including hardware experimental results.

Abbreviations

ACS	AC Switches	OBC	Onboard Charger
AR	Active Rectifier	PP	Parallel-Parallel
AWG	Americal Wire Gauge	PS	Parallel-Series
AGV	Automated Guided Vehicles	PR	Passive Rectifier
AMRs	Automated Mobile Robots	PE	Power Electronics
BDD	Bipolar Double D	PFC	Power Factor Correction
BP	Bipolar Pads	PWM	Pulse Width Modulation
CPT	Capacitive Power Transfer	RX	Receiver
CC	Constant Current	S-BAR	Semi-Bridgeless Active Rectifier
CP	Constant Power	SP	Series Parallel
CV	Constant Voltage	SS	Series–Series
CDR	Current Double Rectifiers	S/SP	Series/Series–Parallel
CDSR	Current Double Synchronous Rectifier	SCCs	Switched-Controlled Capacitors
DDQ	DD-Quadrature	TX	Transmitter
DOF	Degree of Freedom	UAV	Unmanned Air Vehicles
DD	Double D	V2G	Vehicle to Grid
EV	Electric Vehicles	WPT	Wireless Power Transfer
ESR	Equivalent Series Resistance	ZCS	Zero Current Switching
FHA	Fundamental Harmonic Approximation	ZPA	Zero Phase Angle
G2V	Grid to Vehicle	ZVS	Zero Voltage Switching
HFI	High Frequency Inverter		
IPT	Inductive Power Transfer		
ICE	Internal Combustion Engine		
ICCDR	Inverse Coupled Current Double Rectifier		
LEV	Light Electric Vehicles		
Li-ion	Lithium Ion		
MET	Maximum efficiency tracking		

References

1. Roth, H.; Kuhn, P.; Gohla-Neudecker, B. Sustainable Mobility—Cost-Effective and Zero Emission Integration of Germany's Ev Fleet. In Proceedings of the 2009 International Conference on Clean Electrical Power, ICCEP 2009, Capri, Italy, 9–11 June 2009; pp. 207–211. [CrossRef]
2. Bi, Z.; Kan, T.; Mi, C.C.; Zhang, Y.; Zhao, Z.; Keoleian, G.A. A Review of Wireless Power Transfer for Electric Vehicles: Prospects to Enhance Sustainable Mobility. *Appl. Energy* **2016**, *179*, 413–425. [CrossRef]
3. Bindra, A. Electric Vehicle Batteries Eye Solid-State Technology: Prototypes Promise Lower Cost, Faster Charging, and Greater Safety. *IEEE Power Electron. Mag.* **2020**, *7*, 16–19. [CrossRef]
4. Yilmaz, M.; Krein, P.T. Review of Battery Charger Topologies, Charging Power Levels, and Infrastructure for Plug-in Electric and Hybrid Vehicles. *IEEE Trans. Power Electron.* **2013**, *28*, 2151–2169. [CrossRef]

5. Patil, D.; McDonough, M.K.; Miller, J.M.; Fahimi, B.; Balsara, P.T. Wireless Power Transfer for Vehicular Applications: Overview and Challenges. *IEEE Trans. Transp. Electrif.* **2017**, *4*, 3–37. [CrossRef]

6. Tesla, N. Apparatus for Transmission of Electrical Energy. *ACM SIGGRAPH Comput. Graph.* **1900**, *28*, 131–134.

7. Zhang, H.; Lu, F.; Hofmann, H.; Liu, W.; Mi, C.C. A Four-Plate Compact Capacitive Coupler Design and LCL-Compensated Topology for Capacitive Power Transfer in Electric Vehicle Charging Application. *IEEE Trans. Power Electron.* **2016**, *31*, 8541–8551. [CrossRef]

8. Hossain, A.N.M.S.; Erfani, R.; Mohseni, P.; Lavasani, H.M. On the Non-Idealities of a Capacitive Link for Wireless Power Transfer to Biomedical Implants. *IEEE Trans. Biomed. Circuits Syst.* **2021**, *15*, 314–325. [CrossRef]

9. Dai, J.; Ludois, D.C. A Survey of Wireless Power Transfer and a Critical Comparison of Inductive and Capacitive Coupling for Small Gap Applications. *IEEE Trans. Power Electron.* **2015**, *30*, 6017–6029. [CrossRef]

10. Fu, M.; Zhang, T.; Ma, C.; Zhu, X. Efficiency and Optimal Loads Analysis for Multiple-Receiver Wireless Power Transfer Systems. *IEEE Trans. Microw. Theory Tech.* **2015**, *63*, 801–812. [CrossRef]

11. Ahn, D.; Hong, S. Effect of Coupling between Multiple Transmitters or Multiple Receivers on Wireless Power Transfer. *IEEE Trans. Ind. Electron.* **2013**, *60*, 2602–2613. [CrossRef]

12. Bagchi, A.C.; Kamineni, A.; Zane, R.A.; Carlson, R. Review and Comparative Analysis of Topologies and Control Methods in Dynamic Wireless Charging of Electric Vehicles. *IEEE J. Emerg. Sel. Top. Power Electron.* **2021**, *9*, 4947–4962. [CrossRef]

13. Kurs, A.; Karalis, A.; Moffatt, R.; Joannopoulos, J.D.; Fisher, P.; Soljačić, M. Wireless Power Transfer via Strongly Coupled Magnetic Resonances. *Science* **2007**, *317*, 83–86. [CrossRef]

14. Budhia, M.; Covic, G.A.; Boys, J.T. Design and Optimization of Circular Magnetic Structures for Lumped Inductive Power Transfer Systems. *IEEE Trans. Power Electron.* **2011**, *26*, 3096–3108. [CrossRef]

15. Chen, Y.; Zhang, H.; Shin, C.S.; Jo, C.H.; Park, S.J.; Kim, D.H. An Efficiency Optimization-Based Asymmetric Tuning Method of Double-Sided LCC Compensated WPT System for Electric Vehicles. *IEEE Trans. Power Electron.* **2020**, *35*, 11475–11487. [CrossRef]

16. Budhia, M.; Boys, J.T.; Covic, G.A.; Huang, C.Y. Development of a Single-Sided Flux Magnetic Coupler for Electric Vehicle IPT Charging Systems. *IEEE Trans. Ind. Electron.* **2013**, *60*, 318–328. [CrossRef]

17. Jayalath, S.; Khan, A. Design, Challenges, and Trends of Inductive Power Transfer Couplers for Electric Vehicles: A Review. *IEEE J. Emerg. Sel. Top. Power Electron.* **2021**, *9*, 6196–6218. [CrossRef]

18. Micro Electric Vehicles [EV] Market Size | Industry Analysis. Available online: https://www.fortunebusinessinsights.com/micro-electric-vehicles-ev-market-103474 (accessed on 21 February 2023).

19. Voitures Neuves | Constructeur Automobile | Citroën. Available online: https://www.citroen.be/fr/ (accessed on 21 February 2023).

20. Renault TWIZY. Available online: https://nl.renault.be/elektrische-wagens/twizy.html (accessed on 30 September 2022).

21. Specs_E2_Polaris GEM. Available online: https://gem.polaris.com/en-us/e2/specs/ (accessed on 30 September 2022).

22. Liberty | E-Z-GO. Available online: https://ezgo.txtsv.com/personal/golfcarts/liberty (accessed on 21 February 2023).

23. Italcar Industrial | Electric Vehicles. Available online: https://italcar.com/en/homepage/ (accessed on 21 February 2023).

24. Specs: 2022 Polaris RANGER EV Avalanche Gray. Available online: https://www.polaris.com/en-us/off-road/ranger/2022/ranger-ev-avalanche-gray/specs/ (accessed on 22 February 2023).

25. Club Car | World's Best Golf Carts and Utility Vehicles. Available online: https://www.clubcar.com/en-be (accessed on 21 February 2023).

26. Elektro-Gabelstapler—SolidHub. Available online: https://www.solidhub.eu/elektro-gabelstapler/ (accessed on 21 February 2023).

27. Discover the Carver—Carver. Available online: https://carver.earth/en/discover-the-carver/ (accessed on 14 March 2023).

28. This Is Not a Car! | Microlino—Microlino-Car.Com. Available online: https://microlino-car.com/en/microlino (accessed on 13 March 2023).

29. New Baojun Automobile_Baojun Automobile_Wuling Automobile_SAIC-GM-Wuling SGMW Official Website. Available online: https://www.sgmw.com.cn/ (accessed on 12 March 2023).

30. 2020 Toyota C+pod 9.06 KWh (13 Hp) | Technical Specs, Data, Fuel Consumption, Dimensions. Available online: https://www.auto-data.net/en/toyota-c-pod-9.06-kwh-13hp-42028 (accessed on 14 March 2023).

31. Solar Car City Car for Daily Urban Mobility. Available online: https://www.squadmobility.com/# (accessed on 14 March 2023).

32. Home—Triggo. Available online: https://www.triggo.city/ (accessed on 14 March 2023).

33. Eli ZERO | Specs. Available online: https://www.eli.world/specs (accessed on 14 March 2023).

34. Dörsam, T.; Kehl, S.; Klinkig, A.; Radon, A.; Sirch, O. The New Voltage Level 48 V for Vehicle Power Supply. *ATZelektronik Worldw.* **2012**, *7*, 10–15. [CrossRef]

35. Baumgardt, A.; Bachheibl, F.; Patzak, A.; Gerling, D.; Machine, A.E. 48V Traction: Innovative Drive Topology and Battery. In Proceedings of the 2016 IEEE International Conference on Power Electronics, Drives and Energy Systems (PEDES), Trivandrum, India, 14–17 December 2016; pp. 1–6.

36. Haller, S.; Alam, M.F.; Bertilsson, K. Reconfigurable Battery for Charging 48 V EVs in High-Voltage Infrastructure. *Electronics* **2022**, *11*, 353. [CrossRef]

37. Yamamoto, K.; Ponchant, M.; Sellier, F.; Favilli, T.; Pugi, L.; Berzi, L. 48V Electric Vehicle Powertrain Optimal Model-Based Design Methodology. In Proceedings of the 2020 AEIT International Conference of Electrical and Electronic Technologies for Automotive, AEIT AUTOMOTIVE 2020, Turin, Italy, 18–20 November 2020. [CrossRef]

38. Electric Vehicle Powertrain: The 48V Design Challenge | Automotive | Avnet Abacus. Available online: https://www.avnet.com/wps/portal/abacus/solutions/markets/automotive-and-transportation/automotive/power-train-and-ev-hc-phev-systems/the-48v-design-challenge/ (accessed on 21 February 2023).

39. Daszczuk, W.B. Measures of Structure and Operation of Automated Transit Networks. *IEEE Trans. Intell. Transp. Syst.* **2019**, *21*, 2966–2979. [CrossRef]

40. Mercy, T.; Van Parys, R.; Pipeleers, G. Spline-Based Motion Planning for Autonomous Guided Vehicles in a Dynamic Environment. *IEEE Trans. Control. Syst. Technol.* **2018**, *26*, 2182–2189. [CrossRef]

41. Zhu, C.; Yu, J.; Gu, Y.; Gao, J.; Yang, H.; Mai, R.; Li, Y.; He, Z. Analysis and Design of Cost-Effective WPT Systems with Dual Independently Regulatable Outputs for Automatic Guided Vehicles. *IEEE Trans. Power Electron.* **2021**, *36*, 6183–6187. [CrossRef]

42. Nguyen, H.T.; Alsawalhi, J.Y.; Al-Hosani, K.; Al-Sumaiti, A.S.; Al Jaafari, K.A.; Byon, Y.J.; Moursi, M.S. El Review Map of Comparative Designs for Wireless High-Power Transfer Systems in EV Applications: Maximum Efficiency, ZPA, and CC/CV Modes at Fixed Resonance Frequency Independent from Coupling Coefficient. *IEEE Trans. Power Electron.* **2022**, *37*, 4857–4876. [CrossRef]

43. Zhang, Y. Design of High-Power Static Wireless Power Transfer via Magnetic Induction: An Overview. *CPSS Trans. Power Electron. Appl.* **2021**, *6*, 281–297. [CrossRef]

44. Zhang, W.; Mi, C.C. Compensation Topologies of High-Power Wireless Power Transfer Systems. *IEEE Trans. Veh. Technol.* **2016**, *65*, 4768–4778. [CrossRef]

45. Feng, H.; Tavakoli, R.; Onar, O.C.; Pantic, Z. Advances in High-Power Wireless Charging Systems: Overview and Design Considerations. *IEEE Trans. Transp. Electrif.* **2020**, *6*, 886–919. [CrossRef]

46. Raabe, S.; Elliott, G.A.J.; Covic, G.A.; Boys, J.T. A Quadrature Pickup for Inductive Power Transfer Systems. In Proceedings of the ICIEA 2007: 2007 Second IEEE Conference on Industrial Electronics and Applications, Harbin, China, 23–25 May 2007; pp. 68–73. [CrossRef]

47. Zaheer, A.; Kacprzak, D.; Covic, G.A. A Bipolar Receiver Pad in a Lumped IPT System for Electric Vehicle Charging Applications. In Proceedings of the 2012 IEEE Energy Conversion Congress and Exposition, ECCE 2012, Raleigh, NC, USA, 15–20 September 2012; pp. 283–290. [CrossRef]

48. Ding, W. Magnetically Coupled Resonant Using Mn-Zn Ferrite for Wireless Power Transfer. In Proceedings of the 2014 15th International Conference on Electronic Packaging Technology, Chengdu, China, 12–15 August 2014; pp. 1561–1564.

49. Onar, O.C.; Su, G.J.; Asa, E.; Pries, J.; Galigekere, V.; Seiber, L.; White, C.; Wiles, R.; Wilkins, J. 20-KW Bi-Directional Wireless Power Transfer System with Energy Storage System Connectivity. In Proceedings of the IEEE Applied Power Electronics Conference and Exposition—APEC, New Orleans, LA, USA, 15–19 March 2020; pp. 3208–3214. [CrossRef]

50. Bosshard, R.; Member, S.; Kolar, J.W.; Mühlethaler, J.; Member, S.; Wunsch, B. Modeling and η-α-Pareto Optimization of Inductive Power Transfer Coils for Electric Vehicles. *IEEE J. Emerg. Sel. Top. Power Electron.* **2015**, *3*, 50–64. [CrossRef]

51. Kalwar, K.A.; Aamir, M.; Mekhilef, S. Inductively Coupled Power Transfer (ICPT) for Electric Vehicle Charging—A Review. *Renew. Sustain. Energy Rev.* **2015**, *47*, 462–475. [CrossRef]

52. International Commission on Non-Ionizing Radiation Protection. Guidelines for limiting exposure to timevarying electric and magnetic fields (1 Hz to 100 KHz). *Health Phys.* **2020**, *99*, 818–836.

53. Shi, X.; Qi, C.; Qu, M.; Ye, S.; Wang, G.; Sun, L.; Yu, Z. Effects of Coil Shapes on Wireless Power Transfer via Magnetic Resonance Coupling. *J Electromagn. Waves Appl.* **2014**, *28*, 1316–1324. [CrossRef]

54. Miller, J.M.; Daga, A. Elements of Wireless Power Transfer Essential to High Power Charging of Heavy Duty Vehicles. *IEEE Trans. Transp. Electrif.* **2015**, *1*, 26–39. [CrossRef]

55. Kim, J.; Kim, J.; Kong, S.; Kim, H.; Suh, I.S.; Suh, N.P.; Cho, D.H.; Kim, J.; Ahn, S. Coil Design and Shielding Methods for a Magnetic Resonant Wireless Power Transfer System. *Proc. IEEE* **2013**, *101*, 1332–1342. [CrossRef]

56. Budhia, M.; Covic, G.A.; Boys, J.T.; Huang, C.Y. Development and Evaluation of Single Sided Flux Couplers for Contactless Electric Vehicle Charging. In Proceedings of the IEEE Energy Conversion Congress and Exposition: Energy Conversion Innovation for a Clean Energy Future, ECCE 2011, Phoenix, AZ, USA, 17–22 September 2011; pp. 614–621. [CrossRef]

57. Lin, F.Y.; Kim, S.; Covic, G.A.; Boys, J.T. Effective Coupling Factors for Series and Parallel Tuned Secondaries in IPT Systems Using Bipolar Primary Pads. *IEEE Trans. Transp. Electrif.* **2017**, *3*, 434–444. [CrossRef]

58. Covic, G.A.; Boys, J.T. Modern Trends in Inductive Power Transfer for Transportation Applications. *IEEE J. Emerg. Sel. Top. Power Electron.* **2013**, *1*, 28–41. [CrossRef]

59. Chopra, S.; Bauer, P. Analysis and Design Considerations for a Contactless Power Transfer System. In Proceedings of the INTELEC, International Telecommunications Energy Conference, Amsterdam, The Netherlands, 9–13 October 2011. [CrossRef]

60. Wang, C.S.; Covic, G.A.; Stielau, O.H. Power Transfer Capability and Bifurcation Phenomena of Loosely Coupled Inductive Power Transfer Systems. *IEEE Trans. Ind. Electron.* **2004**, *51*, 148–157. [CrossRef]

61. Outeiro, M.T.; Buja, G.; Czarkowski, D. Resonant Power Converters: An Overview with Multiple Elements in the Resonant Tank Network. *IEEE Ind. Electron. Mag.* **2016**, *10*, 21–45. [CrossRef]

62. Keeling, N.A.; Covic, G.A.; Boys, J.T. A Unity-Power-Factor IPT Pickup for High-Power Applications. *IEEE Trans. Ind. Electron.* **2010**, *57*, 744–751. [CrossRef]

63. Ke, G.; Chen, Q.; Gao, W.; Wong, S.C.; Tse, C.K.; Zhang, Z. Research on IPT Resonant Converters with High Misalignment Tolerance Using Multicoil Receiver Set. *IEEE Trans. Power Electron.* **2020**, *35*, 3697–3712. [CrossRef]

64. Zhang, W.; Wong, S.C.; Tse, C.K.; Chen, Q. Load-Independent Duality of Current and Voltage Outputs of a Series- or Parallel-Compensated Inductive Power Transfer Converter with Optimized Efficiency. *IEEE J. Emerg. Sel. Top. Power Electron.* **2015**, *3*, 137–146. [CrossRef]

65. Qu, X.; Han, H.; Wong, S.C.; Tse, C.K.; Chen, W. Hybrid IPT Topologies with Constant Current or Constant Voltage Output for Battery Charging Applications. *IEEE Trans. Power Electron.* **2015**, *30*, 6329–6337. [CrossRef]

66. Huang, Z.; Wong, S.C.; Tse, C.K. Design of a Single-Stage Inductive-Power-Transfer Converter for Efficient EV Battery Charging. *IEEE Trans. Veh. Technol.* **2017**, *66*, 5808–5821. [CrossRef]

67. Huang, Z.; Wong, S.C.; Tse, C.K. An Inductive-Power-Transfer Converter with High Efficiency Throughout Battery-Charging Process. *IEEE Trans. Power Electron.* **2019**, *34*, 10245–10255. [CrossRef]

68. Auvigne, C.; Germano, P.; Ladas, D.; Perriard, Y. A Dual-Topology ICPT Applied to an Electric Vehicle Battery Charger. In Proceedings of the 2012 20th International Conference on Electrical Machines, ICEM 2012, Marseille, France, 2–5 September 2012; pp. 2287–2292. [CrossRef]

69. Villa, J.L.; Sallán, J.; Sanz Osorio, J.F.; Llombart, A. High-Misalignment Tolerant Compensation Topology for ICPT Systems. *IEEE Trans. Ind. Electron.* **2012**, *59*, 945–951. [CrossRef]

70. Hou, J.; Chen, Q.; Wong, S.C.; Tse, C.K.; Ruan, X. Analysis and Control of Series/Series-Parallel Compensated Resonant Converter for Contactless Power Transfer. *IEEE J. Emerg. Sel. Top. Power Electron.* **2015**, *3*, 124–136. [CrossRef]

71. Hou, J.; Chen, Q.; Ren, X.; Ruan, X.; Wong, S.C.; Tse, C.K. Precise Characteristics Analysis of Series/Series-Parallel Compensated Contactless Resonant Converter. *IEEE J. Emerg. Sel. Top. Power Electron.* **2015**, *3*, 101–110. [CrossRef]

72. Yao, Y.; Wang, Y.; Liu, X.; Lu, K.; Xu, D. Analysis and Design of an S/SP Compensated IPT System to Minimize Output Voltage Fluctuation versus Coupling Coefficient and Load Variation. *IEEE Trans. Veh. Technol.* **2018**, *67*, 9262–9272. [CrossRef]

73. Lu, J.; Zhu, G.; Lin, D.; Zhang, Y.; Wang, H.; Mi, C.C. Realizing Constant Current and Constant Voltage Outputs and Input Zero Phase Angle of Wireless Power Transfer Systems with Minimum Component Counts. *IEEE Trans. Intell. Transp. Syst.* **2021**, *22*, 600–610. [CrossRef]

74. Wang, Y.; Zhao, S.; Zhang, H.; Lu, F. High-Efficiency Bilateral S–SP Compensated Multiload IPT System with Constant-Voltage Outputs. *IEEE Trans. Industr. Inform.* **2022**, *18*, 901–910. [CrossRef]

75. Madawala, U.K.; Thrimawithana, D.J. A Bidirectional Inductive Power Interface for Electric Vehicles in V2G Systems. *IEEE Trans. Ind. Electron.* **2011**, *58*, 4789–4796. [CrossRef]

76. Qu, X.; Chu, H.; Huang, Z.; Wong, S.C.; Tse, C.K.; Mi, C.C.; Chen, X. Wide Design Range of Constant Output Current Using Double-Sided LC Compensation Circuits for Inductive-Power-Transfer Applications. *IEEE Trans. Power Electron.* **2019**, *34*, 2364–2374. [CrossRef]

77. Shi, G.; Guo, W.; Liul, X.; Wang, Y.; Yaol, Y.; Xul, D. A Double-T-Type Compensation Network and Its Tuning Method for IPT System. In Proceedings of the IEEE International Conference on Power Electronics, Drives and Energy Systems, PEDES 2016, Trivandrum, India, 14–17 December 2016; pp. 1–5. [CrossRef]

78. Zhang, Z.; Zheng, S.; Luo, S.; Xu, D.; Krein, P.T.; Ma, H. An Inductive Power Transfer Charging System with a Multiband Frequency Tracking Control for Misalignment Tolerance. *IEEE Trans. Power Electron.* **2022**, *37*, 11342–11355. [CrossRef]

79. Tran, M.T.; Choi, W. Design and Implementation of a Constant Current and Constant Voltage Wireless Charger Operating at 6.78 MHz. *IEEE Access* **2019**, *7*, 184254–184265. [CrossRef]

80. Wang, X.; Xu, J.; Leng, M.; Ma, H.; He, S. A Hybrid Control Strategy of LCC-S Compensated WPT System for Wide Output Voltage and ZVS Range with Minimized Reactive Current. *IEEE Trans. Ind. Electron.* **2021**, *68*, 7908–7920. [CrossRef]

81. Kim, M.; Joo, D.M.; Lee, B.K. Design and Control of Inductive Power Transfer System for Electric Vehicles Considering Wide Variation of Output Voltage and Coupling Coefficient. *IEEE Trans. Power Electron.* **2019**, *34*, 1197–1208. [CrossRef]

82. Yan, Z.; Zhang, Y.; Song, B.; Zhang, K.; Kan, T.; Mi, C. An LCC-p Compensated Wireless Power Transfer System with a Constant Current Output and Reduced Receiver Size. *Energies* **2019**, *12*, 172. [CrossRef]

83. Vu, V.B.; Phan, V.T.; Dahidah, M.; Pickert, V. Multiple Output Inductive Charger for Electric Vehicles. *IEEE Trans. Power Electron.* **2019**, *34*, 7350–7368. [CrossRef]

84. Kavimandan, U.D.; Galigekere, V.P.; Onar, O.; Mohammad, M.; Ozpineci, B.; Mahajan, S.M. The Sensitivity Analysis of Coil Misalignment for a 200-KW Dynamic Wireless Power Transfer System with an LCC-S and LCC-P Compensation. In Proceedings of the 2021 IEEE Transportation Electrification Conference and Expo, ITEC 2021, Chicago, IL, USA, 21–25 June 2021; pp. 1–8. [CrossRef]

85. Hou, J.; Chen, Q.; Zhang, Z.; Wong, S.C.; Tse, C.K. Analysis of Output Current Characteristics for Higher Order Primary Compensation in Inductive Power Transfer Systems. *IEEE Trans. Power Electron.* **2018**, *33*, 6807–6821. [CrossRef]

86. Wu, H.H.; Gilchrist, A.; Sealy, K.D.; Bronson, D. A High Efficiency 5 KW Inductive Charger for EVs Using Dual Side Control. *IEEE Trans. Ind. Inform.* **2012**, *8*, 585–595. [CrossRef]

87. Li, S.; Li, W.; Deng, J.; Nguyen, T.D.; Mi, C.C. A Double-Sided LCC Compensation Network and Its Tuning Method for Wireless Power Transfer. *IEEE Trans. Veh. Technol.* **2015**, *64*, 2261–2273. [CrossRef]

88. Li, W.; Zhao, H.; Li, S.; Deng, J.; Kan, T.; Mi, C.C. Integrated LCC Compensation Topology for Wireless Charger in Electric and Plug-in Electric Vehicles. *IEEE Trans. Ind. Electron.* **2015**, *62*, 4215–4225. [CrossRef]
89. Qu, X.; Chu, H.; Wong, S.C.; Tse, C.K. An IPT Battery Charger with Near Unity Power Factor and Load-Independent Constant Output Combating Design Constraints of Input Voltage and Transformer Parameters. *IEEE Trans. Power Electron.* **2019**, *34*, 7719–7727. [CrossRef]
90. Vu, V.B.; Tran, D.H.; Choi, W. Implementation of the Constant Current and Constant Voltage Charge of Inductive Power Transfer Systems with the Double-Sided LCC Compensation Topology for Electric Vehicle Battery Charge Applications. *IEEE Trans. Power Electron.* **2018**, *33*, 7398–7410. [CrossRef]
91. Kan, T.; Nguyen, T.D.; White, J.C.; Malhan, R.K.; Mi, C.C. A New Integration Method for an Electric Vehicle Wireless Charging System Using LCC Compensation Topology: Analysis and Design. *IEEE Trans. Power Electron.* **2017**, *32*, 1638–1650. [CrossRef]
92. Mai, R.; Chen, Y.; Li, Y.; Zhang, Y.; Cao, G.; He, Z. Inductive Power Transfer for Massive Electric Bicycles Charging Based on Hybrid Topology Switching with a Single Inverter. *IEEE Trans. Power Electron.* **2017**, *32*, 5897–5906. [CrossRef]
93. Hwang, S.H.; Chen, Y.; Zhang, H.; Lee, K.Y.; Kim, D.H. Reconfigurable Hybrid Resonant Topology for Constant Current/Voltage Wireless Power Transfer of Electric Vehicles. *Electronics* **2020**, *9*, 1323. [CrossRef]
94. Wang, D.; Qu, X.; Yao, Y.; Yang, P. Hybrid Inductive-Power-Transfer Battery Chargers for Electric Vehicle Onboard Charging with Configurable Charging Profile. *IEEE Trans. Intell. Transp. Syst.* **2021**, *22*, 592–599. [CrossRef]
95. Tuan, T.M.; Choi, W. A 6.78 MHz Constant Current and Constant Voltage Wireless Charger for E-Mobility Applications. In Proceedings of the KIPE Conference, Busan, Republic of Korea, 27–30 May 2019; pp. 142–144.
96. Chen, Y.; Yang, B.; Kou, Z.; He, Z.; Cao, G.; Mai, R. Hybrid and Reconfigurable IPT Systems with High-Misalignment Tolerance for Constant-Current and Constant-Voltage Battery Charging. *IEEE Trans. Power Electron.* **2018**, *33*, 8259–8269. [CrossRef]
97. Zhang, Y.; Kan, T.; Yan, Z.; Mi, C.C. Frequency and Voltage Tuning of Series-Series Compensated Wireless Power Transfer System to Sustain Rated Power under Various Conditions. *IEEE J. Emerg. Sel. Top. Power Electron.* **2019**, *7*, 1311–1317. [CrossRef]
98. Koran, A.; Badran, K. Adaptive Frequency Control of a Sensorless-Receiver Inductive Wireless Power Transfer System Based on Mixed-Compensation Topology. *IEEE Trans. Power Electron.* **2021**, *36*, 978–990. [CrossRef]
99. Song, K.; Li, Z.; Jiang, J.; Zhu, C. Constant Current/Voltage Charging Operation for Series-Series and Series-Parallel Compensated Wireless Power Transfer Systems Employing Primary-Side Controller. *IEEE Trans. Power Electron.* **2018**, *33*, 8065–8080. [CrossRef]
100. Rong, C.; Zhang, B.; Jiang, Y.; Shu, X.; Wei, Z. A Misalignment-Tolerant Fractional-Order Wireless Charging System With Constant Current or Voltage Output. *IEEE Trans. Power Electron.* **2022**, *37*, 11356–11368. [CrossRef]
101. Yenil, V.; Cetin, S. Load Independent Constant Current and Constant Voltage Control of LCC-Series Compensated Wireless EV Charger. *IEEE Trans. Power Electron.* **2022**, *37*, 8701–8712. [CrossRef]
102. Jiang, Y.; Wang, L.; Fang, J.; Li, R.; Han, R.; Wang, Y. A High-Efficiency ZVS Wireless Power Transfer System for Electric Vehicle Charging with Variable Angle Phase Shift Control. *IEEE J. Emerg. Sel. Top. Power Electron.* **2021**, *9*, 2356–2372. [CrossRef]
103. Diekhans, T.; De Doncker, R.W. A Dual-Side Controlled Inductive Power Transfer System Optimized for Large Coupling Factor Variations and Partial Load. *IEEE Trans. Power Electron.* **2015**, *30*, 6320–6328. [CrossRef]
104. Jiang, Y.; Wang, L.; Wang, Y.; Wu, M.; Zeng, Z.; Liu, Y.; Sun, J. Phase-Locked Loop Combined with Chained Trigger Mode Used for Impedance Matching in Wireless High Power Transfer. *IEEE Trans. Power Electron.* **2020**, *35*, 4272–4285. [CrossRef]
105. Chen, C.; Zhou, H.; Deng, Q.; Hu, W.; Yu, Y.; Lu, X.; Lai, J. Modeling and Decoupled Control of Inductive Power Transfer to Implement Constant Current/Voltage Charging and ZVS Operating for Electric Vehicles. *IEEE Access* **2018**, *6*, 59917–59928. [CrossRef]
106. Orekan, T.; Zhang, P.; Shih, C. Analysis, Design, and Maximum Power-Efficiency Tracking for Undersea Wireless Power Transfer. *IEEE J. Emerg. Sel. Top. Power Electron.* **2018**, *6*, 843–854. [CrossRef]
107. Yang, Y.; Zhong, W.; Kiratipongvoot, S.; Tan, S.C.; Hui, S.Y.R. Dynamic Improvement of Series-Series Compensated Wireless Power Transfer Systems Using Discrete Sliding Mode Control. *IEEE Trans. Power Electron.* **2018**, *33*, 6351–6360. [CrossRef]
108. Zhong, W.X.; Hui, S.Y.R. Maximum Energy Efficiency Tracking for Wireless Power Transfer Systems. *IEEE Trans. Power Electron.* **2015**, *30*, 4025–4034. [CrossRef]
109. Li, H.; Li, J.; Wang, K.; Chen, W.; Yang, X. A Maximum Efficiency Point Tracking Control Scheme for Wireless Power Transfer Systems Using Magnetic Resonant Coupling. *IEEE Trans. Power Electron.* **2015**, *30*, 3998–4008. [CrossRef]
110. Dai, X.; Li, X.; Li, Y.; Hu, A.P. Maximum Efficiency Tracking for Wireless Power Transfer Systems with Dynamic Coupling Coefficient Estimation. *IEEE Trans. Power Electron.* **2018**, *33*, 5005–5015. [CrossRef]
111. Yang, L.; Shi, Y.; Wang, M.; Ren, L. Constant Voltage Charging and Maximum Efficiency Tracking for WPT Systems Employing Dual-Side Control Scheme. *IEEE J. Emerg. Sel. Top. Power Electron.* **2022**, *10*, 945–955. [CrossRef]
112. Lu, J.; Zhu, G.; Lin, D.; Zhang, Y.; Jiang, J.; Mi, C.C. Unified Load-Independent ZPA Analysis and Design in CC and CV Modes of Higher Order Resonant Circuits for WPT Systems. *IEEE Trans. Transp. Electrif.* **2019**, *5*, 977–987. [CrossRef]
113. Wang, X.; Xu, J.; Ma, H.; He, S. Inductive Power Transfer Systems with Digital Switch-Controlled Capacitor for Maximum Efficiency Point Tracking. *IEEE Trans. Ind. Electron.* **2021**, *68*, 9467–9480. [CrossRef]
114. Song, K.; Lan, Y.; Wei, R.; Yang, G.; Yang, F.; Li, W.; Jiang, J.; Zhu, C.; Li, Y. A Control Strategy for Wireless EV Charging System to Improve Weak Coupling Output Based on Variable Inductor and Capacitor. *IEEE Trans. Power Electron.* **2022**, *37*, 12853–12864. [CrossRef]

115. Zhang, Z.; Zhu, F.; Xu, D.; Krein, P.T.; Ma, H. An Integrated Inductive Power Transfer System Design with a Variable Inductor for Misalignment Tolerance and Battery Charging Applications. *IEEE Trans. Power Electron.* **2020**, *35*, 11544–11556. [CrossRef]
116. Kavimandan, U.D.; Mahajan, S.M.; Van Neste, C.W. Analysis and Demonstration of a Dynamic ZVS Angle Control Using a Tuning Capacitor in a Wireless Power Transfer System. *IEEE J. Emerg. Sel. Top. Power Electron.* **2021**, *9*, 1876–1890. [CrossRef]
117. Wong, C.S.; Wong, M.C.; Cao, L.; Loo, K.H. Design of High-Efficiency Inductive Charging System with Load-Independent Output Voltage and Current Tolerant of Varying Coupling Condition. *IEEE Trans. Power Electron.* **2021**, *36*, 13546–13561. [CrossRef]
118. Li, W.; Zhang, Q.; Cui, C.; Wei, G. A Self-Tuning S/S Compensation WPT System without Parameter Recognition. *IEEE Trans. Ind. Electron.* **2022**, *69*, 6741–6750. [CrossRef]
119. Luo, Z.; Zhao, Y.; Xiong, M.; Wei, X.; Dai, H. A Self-Tuning LCC/LCC System Based on Switch-Controlled Capacitors for Constant-Power Wireless Electric Vehicle Charging. *IEEE Trans. Ind. Electron.* **2022**, *70*, 709–720. [CrossRef]
120. Lim, Y.; Tang, H.; Lim, S.; Park, J. An Adaptive Impedance-Matching Network Based on a Novel Capacitor Matrix for Wireless Power Transfer. *IEEE Trans. Power Electron.* **2014**, *29*, 4403–4413. [CrossRef]
121. Zhang, Z.; Ai, W.; Liang, Z.; Wang, J. Topology-Reconfigurable Capacitor Matrix for Encrypted Dynamic Wireless Charging of Electric Vehicles. *IEEE Trans. Veh. Technol.* **2018**, *67*, 9284–9293. [CrossRef]
122. Lee, E.S.; Han, S.H. 2-D Thin Coil Designs of IPT for Wireless Charging of Automated Guided Vehicles. *IEEE J. Emerg. Sel. Top. Power Electron.* **2022**, *10*, 2629–2644. [CrossRef]
123. Lu, F.; Zhang, H.; Zhu, C.; Diao, L.; Gong, M.; Zhang, W.; Mi, C.C. A Tightly Coupled Inductive Power Transfer System for Low-Voltage and High-Current Charging of Automatic Guided Vehicles. *IEEE Trans. Ind. Electron.* **2019**, *66*, 6867–6875. [CrossRef]
124. Lu, F.; Zhang, Y.; Zhang, H.; Zhu, C.; Diao, L.; Gong, M.; Zhang, W.; Mi, C. A Low-Voltage and High-Current Inductive Power Transfer System with Low Harmonics for Automatic Guided Vehicles. *IEEE Trans. Veh. Technol.* **2019**, *68*, 3351–3360. [CrossRef]
125. Zaheer, A.; Covic, G.A.; Kacprzak, D. A Bipolar Pad in a 10-KHz 300-W Distributed IPT System for AGV Applications. *IEEE Trans. Ind. Electron.* **2014**, *61*, 3288–3301. [CrossRef]
126. Liu, S.; Zhao, X.; Wu, Y.; Zhou, L.; Li, Y.; Mai, R.; He, Z. Efficiency Improvement of Dual-Receiver WPT Systems Based on Partial Power Processing Control. *IEEE Trans. Power Electron.* **2022**, *37*, 7456–7469. [CrossRef]
127. Shi, L.; Delgado, A.; Ramos, R.; Alou, P. A Wireless Power Transfer System with Inverse Coupled Current Doubler Rectifier for High-Output Current Applications. *IEEE Trans. Ind. Electron.* **2022**, *69*, 4607–4616. [CrossRef]
128. Li, Y.; Lin, T.; Mai, R.; Huang, L.; He, Z. Compact Double-Sided Decoupled Coils-Based WPT Systems for High-Power Applications: Analysis, Design, and Experimental Verification. *IEEE Trans. Transp. Electrif.* **2017**, *4*, 64–75. [CrossRef]
129. Pan, S.; Xu, Y.; Lu, Y.; Liu, W.; Li, Y.; Mai, R. Design of Compact Magnetic Coupler with Low Leakage EMF for AGV Wireless Power Transfer System. *IEEE Trans. Ind. Appl.* **2022**, *58*, 1044–1052. [CrossRef]
130. Wu, T.F.; Tsai, C.T.; Chang, Y.D.; Chen, Y.M. Analysis and Implementation of an Improved Current-Doubler Rectifier with Coupled Inductors. *IEEE Trans. Power Electron.* **2008**, *23*, 2681–2693. [CrossRef]
131. Badstuebner, U.; Biela, J.; Christen, D.; Kolar, J.W. Optimization of a 5-KW Telecom Phase-Shift Dc-Dc Converter with Magnetically Integrated Current Doubler. *IEEE Trans. Ind. Electron.* **2011**, *58*, 4736–4745. [CrossRef]
132. Shin, J.Y.; Kim, H.W.; Cho, K.Y.; Hwang, S.S.; Chung, S.K.; Chung, G.B. Analysis of LLC Resonant Converter with Current-Doubler Rectification Circuit. In Proceedings of the 16th International Power Electronics and Motion Control Conference and Exposition, PEMC 2014, Antalya, Turkey, 21–24 September 2014; pp. 162–167. [CrossRef]
133. Xiong, M.; Dai, H.; Li, Q.; Jiang, Z.; Luo, Z.; Wei, X. Design of the LCC-SP Topology with a Current Doubler for 11-KW Wireless Charging System of Electric Vehicles. *IEEE Trans. Transp. Electrif.* **2021**, *7*, 2128–2142. [CrossRef]
134. Scortegagna, R.G.; Gules, R. Self-Driven Current-Doubler Synchronous Rectifier and Design Tuning for Maximizing Efficiency in IPT Systems. *IEEE J. Emerg. Sel. Top. Power Electron.* **2022**, *10*, 1007–1016. [CrossRef]
135. Tao, C.; Liu, Z.; Li, S.; Guo, Y.; Wang, L. A High-Efficiency Wireless Power Transfer System Using Quasi-Z-Source Inverter and Current-Double Synchronous Rectifier for Low-Voltage and High-Current Applications. *IEEE Trans. Transp. Electrif.* **2022**, *8*, 2758–2769. [CrossRef]
136. Feng, H.; Lukic, S.M. Reduced-Order Modeling and Design of Single-Stage LCL Compensated IPT System for Low Voltage Vehicle Charging Applications. *IEEE Trans. Veh. Technol.* **2020**, *69*, 3728–3739. [CrossRef]
137. Zhou, L.; Mai, R.; Liu, S.; Yu, J.; Li, Y.; Fu, L. Minimizing Input Current of the Rectifier of LCC-LCC Compensated IPT Systems by Switch-Controlled Capacitor for Improving Efficiency. *IEEE Trans. Ind. Appl.* **2022**, *58*, 1010–1021. [CrossRef]
138. Yang, B.; Lu, Y.; Peng, Y.; He, S.; Chen, Y.; He, Z.; Mai, R.; Wang, Z. Analysis and Design of a T/S Compensated IPT System for AGV Maintaining Stable Output Current Versus Air Gap and Load Variations. *IEEE Trans. Power Electron.* **2022**, *37*, 6217–6228. [CrossRef]
139. Wang, H.; Member, S.; Chen, Y.; Member, S.; Qiu, Y.; Fang, P.; Zhang, Y.; Wang, L.; Liu, Y.; Afsharian, J.; et al. Common Capacitor Multiphase LLC Converter with Passive Current Sharing Ability. *IEEE Trans. Power Electron.* **2018**, *33*, 370–387. [CrossRef]
140. Wang, H.; Member, S.; Chen, Y.; Member, S.; Liu, Y. A Passive Current Sharing Method with Common Inductor Multiphase LLC Resonant Converter. *IEEE Trans. Power Electron.* **2017**, *32*, 6994–7010. [CrossRef]